Effect of fault roughness on aftershock distribution: Plastic off-fault material properties

Khurram S. Aslam,[1] Eric G. Daub[1,2]

Corresponding author: Khurram S. Aslam, Center for Earthquake Research and Information, University of Memphis, Memphis, Tenneessee, USA. (ksaslam@memphis.edu)

[1]Center for Earthquake Research and Information, University of Memphis, Memphis, Tennessee, USA.

[2]Alan Turing Institute, London, United Kingdom.

Abstract.

We perform spontaneous earthquake rupture simulations on rough strike-slip faults with off-fault plastic material properties. We examine the off-fault stress change and damage pattern resulting from dynamic fault slip in the near-fault region. We use the stress output from each simulation to calculate the Coulomb failure function (CFF). We calculate the CFF values on the extensional side of the fault using parallel receiver fault orientations as well as using variable receiver fault orientations determined using the angle at which plastic shear strain is maximum. We calculate and examine the probability density function (PDF) for the CFF values across the fault as a function of distance. We observe that the overall trend of the CFF values with distance remains similar for the extensional and compressional sides - the PDF of CFF shows a broad range of values in the near-fault region and this spread collapses into a narrow range away from the near-fault region, similar to the distribution found for elastic off-fault properties. In the near-fault region, we observe many positive CFF change zones that are potential locations of aftershocks and we calculate their areas and amplitude as a function of distance away from fault. Our comparison of CFF amplitudes as a function of rupture areas suggests that the spatial aftershock distribution surrounding a fault is controlled by both stress heterogeneity as well as the damage zone complexity. The calculations of rupture areas using our model are consistent with ruptured areas of observed aftershocks in California.

1. Introduction

An earthquake causes stress changes in its surrounding region. These induced stress changes can either increase or decrease the seismic activity of that region [*King et al.*, 1994; *Stein*, 2003; *Lin and Stein*, 2004; *Toda et al.*, 1998, 2005; *Stein*, 1999; *Freed*, 2005; *Steacy et al.*, 2005]. This change in seismic activity due to stress changes is referred to as earthquake triggering [*Freed*, 2005]. Understanding the mechanics of aftershock triggering is an important aspect of earthquake science, as an understanding of time-dependent earthquake rates helps constrain the risk they pose to humans and property [*Cocco and Rice*, 2002; *King et al.*, 2001; *Hill et al.*, 2002; *Scholz*, 2002]. Many studies have been dedicated to understanding aftershock triggering and have proposed different triggering mechanisms. These effects include changes in static stress [*King et al.*, 1994; *Stein*, 1999; *Harris and Simpson*, 1992], dynamic stresses from passing seismic waves [*Hill et al.*, 1993; *Gomberg et al.*, 2003; *Pankow et al.*, 2004], aseismic afterslip below a rupture fault plane [*Perfettini and Avouac*, 2004]), fluid pressure variation due to its flow [*Nur and Booker*, 1972] and visco-elastic relaxation in the asthenosphere [*Lippiello et al.*, 2015]. Although all of these mechanisms are believed to play a role in aftershock triggering, the relative importance of each mechanism remains an open issue in earthquake science. Furthermore, the contribution of each of these mechanisms is not straightforward to quantify [*Freed*, 2005; *El Hariri et al.*, 2010; *Vidale et al.*, 2006; *Vidale and Shearer*, 2006].

The static stress changes are calculated based on the Coulomb failure function (CFF) [*King et al.*, 1994; *Freed*, 2005; *Jaeger et al.*, 2009; *Bruhn*, 1990]. The change in normal and shear stresses on a fault determine the Coulomb stress change for that fault. A positive change in Coulomb stress brings a fault closer to failure, while a negative change in Coulomb stress brings a fault away from failure. The static stress changes can explain many features of seismicity such as the spatial distribution of aftershocks and their temporal sequences, and the seismic inactivity after a large earthquake in a seismically active region [*Freed*, 2005]. The static stress change model has been successful in predicting the aftershocks observed within distances of 1-2 fault lengths, but even within this distance, this model is not able to explain the occurrence of aftershocks in stress shadows. For instance, the $M_w = 6.9$ 1989 Loma Prieta Earthquake produced aftershocks in regions of stress shadows within a few fault lengths which cannot be explained by static stress changes [*Segou and Parsons*, 2014].

To better understand the static stress effects induced by an earthquake, we perform spontaneous earthquake rupture simulations of large earthquakes on a geometrically complex fault. Dynamic rupture simulations solve physics-based model of stresses and slip and hence these models can be used to calculate the static stress changes after the dynamic phase of an earthquake, which gives us an estimate of the expected aftershock triggering locations. Spontaneous earthquake rupture simulations have been extensively used by the earthquake science community (both in 2D and 3D) to understand the physical processes that occur during propagation of earthquake rupture [*Aochi et al.*, 2000; *Harris*, 2004; *Bizzarri and Cocco*, 2005; *Dalguer et al.*, 2003; *Daub and Carlson*, 2008, 2010; *Shi and Day*, 2013; *Harris and Day*, 1997; *Dunham and Archuleta*, 2005; *Tinti et al.*, 2005; *Shi and Ben-Zion*, 2006]. An advantage of using dynamic rupture models to calculate static stress changes is its ability to resolve small scale details of slip and stress change when compared to kinematically inverted fault models. These small scale details play an important role in determining the near-fault stress change following an earthquake, particularly since the small scale changes in stresses may change the locations and extent of stress shadows over length scales relevant for the typical rupture lengths of smaller aftershocks.

Our dynamic earthquake rupture simulations consider continuum plasticity [*Andrews*, 2005; *Dunham et al.*, 2011a, b; *Shi and Day*, 2013; *Gabriel et al.*, 2013] to describe the off-fault material. We consider plastic rather than elastic off-fault material properties [*Aslam and Daub*, 2018] in this study since the elastic off-fault material properties may predict extreme stress conditions near the rupture front (e.g [*Noda et al.*, 2009]) which are high enough for the material to deform inelastically [*Dunham et al.*, 2011a, b; *Johri et al.*, 2014; *Shi and Day*, 2013; *Rice et al.*, 2005; *Poliakov et al.*, 2002]. Many recent dynamic earthquake rupture simulation studies have used continuum plasticity to represent off-fault material properties [*Andrews*, 2005; *Ben-Zion and Shi*, 2005; *Duan*, 2008; *Templeton and Rice*, 2008; *Viesca et al.*, 2008; *Dunham et al.*, 2011a, b; *Ma and Beroza*, 2008]. For example, *Andrews* [2005] performed dynamic rupture simulations on a flat fault in 2D with off-fault plasticity and observed that the distribution of plastic strain has a uniform magnitude along the fault while its thickness across the fault is proportional to the distance of rupture propagation. *Ben-Zion and Shi* [2005] performed dynamic rupture simulations in 2D on flat faults with off-fault plasticity and based on the damage observed as a result of different input parameters (normal stress, cohesion, etc.). They noted that the off-fault material damage is significant in the top few kilometers of the crust. *Duan* [2008] performed dynamic rupture simulations in 2D on flat faults with off-fault plasticity to study the effects of a low-velocity fault zone (LVFZ) on the rupture propagation. They observed larger slip rate values due to the presence of LVFZ and significant amplification of ground shaking in areas within the LVFZ region. *Templeton and Rice* [2008] performed dynamic rupture simulations in 2D on flat faults with off-fault plasticity in dry materials to learn how different parameters affect and control the extent of off-fault damage during rupture propagation. *Viesca et al.* [2008] performed similar rupture simulations in fluid-saturated materials to observe how the fluid-saturated material respond to dynamic rupture propagation in comparison to the dry material.

Most of the studies discussed above considered flat faults to perform dynamic rupture simulations. Since real faults are not flat but rather exhibit complex geometries [*Candela et al.*, 2012; *Brown and Scholz*, 1985; *Power et al.*, 1987; *Power and Tullis*, 1995; *Renard et al.*, 2006], considering these heterogeneities of the fault surface is important since a real geological fault with geometrical complexities can introduce significant changes in the stress distribution when the fault slips. These stress perturbations sometimes reach the level of existing tectonic stresses of the area [*Chester and Chester*, 2000; *Dieterich and Smith*, 2009] and have a significant effect on the static stress change in the region surrounding the fault. Many quasi-static modeling studies have considered complex fault geometries in order to calculate the slip distribution and resulting stress changes as a result of failure on the geometrically complex fault [*Smith and Dieterich*, 2010; *Powers and Jordan*, 2010; *Bailey and Ben-Zion*, 2009]. A few recent studies of dynamic rupture have performed dynamic rupture simulations on geometrically complex rough faults (e.g. [*Dunham et al.*, 2011b; *Fang and Dunham*, 2013; *Bruhat et al.*, 2016; *Shi and Day*, 2013; *Johri et al.*, 2014; *Harris et al.*, 2018]) rather than the conventional flat faults to examine the physical processes that occur during propagation of earthquakes for more realistic geometries.

In our previous study [*Aslam and Daub*, 2018], we performed dynamic rupture simulations on rough faults with off-fault elasticity to study the effects of fault roughness on the aftershocks. We found that the extent of the near-fault region of complex static stress changes is mainly controlled by RMS height of the rough fault profile, and the Hurst exponent of the fault profile does not affect the spatial extent of the near-fault region. Our study assumed elastic off-fault material properties, which provided many insights into the point statistics and expected spatial characteristics of the static stress changes. However, these results may not be relevant when extreme stress conditions are encountered that cause the material to deform inelastically. Similarly, all of our calculations of static stress changes were based on the assumption of a predefined single receiver fault orientation, while the orientations of faults in a multi-fault system may not be parallel in general. *Hainzl et al.* [2010] showed that incorporating realistic multiple receiver fault orientations changes the spatial pattern of predicted aftershocks, and the new pattern shows better agreement with observed data (i.e. aftershocks of the 1992 M_w 7.3 Landers earthquake). Although our study addressed the question of relating the spatial distribution of aftershocks with the static stress changes in detail, we did not address the relationship of aftershock seismicity with the damage zone and multiple receiver fault orientations.

This study expands upon our previous work in order to investigate if the stress field or damage zone controls the off-fault seismic activity. We build upon our previous dynamic rupture studies described above and perform numerous two dimensional (2D) earthquake simulations on rough strike slip fault profiles. We quantify the stress changes in the off-fault material due to dynamic slip on the fault where the off-fault material properties are described using plasticity. We use Drucker-Prager visco-plasticity to account for off-fault material failure. We use self similar fault fractal profiles (Hurst exponent = 1), with fault roughness amplitude values of 0.01 to represent our fault profile. These fault roughness values are taken from major strike slip fault observational studies [*Candela et al.*, 2012]. We run our simulations for numerous realizations of the fault profile and then calculate the amplitudes of the CFF for each of these realizations. We calculate the probability density function (PDF) of the CFF from all fault realizations in order to quantify and compare it with the aftershock distributions in space using observational data. We use relocated earthquake catalogs from Northern and Southern California [*Shearer et al.*, 2005; *Waldhauser and Schaff*, 2008] for the comparison of our model results with naturally occurring seismicity.

2. Inelastic off-fault material response and plasticity

Experimental studies show a pressure-dependent yielding in both rocks and soils [*Brace et al.*, 1966; *Hirth and Tullis*, 1992; *Mogi*, 1971, 1974, 1972; *Templeton and Rice*, 2008]. The onset of this inelastic deformation is dependent upon the mean normal stress. In brittle rocks, this deformation occurs as a result of frictional sliding on micro cracks and fractures [*Dunham et al.*, 2011b; *Rudnicki and Rice*, 1975]. We use the Drucker-Prager model to describe this inelastic deformation. This model is similar to the Mohr-Coulomb model and under certain stress states, the yield criterion of both models become equivalent.

Under Drucker-Prager viscoplasticity, the material flows when stresses exceed the yield function $F(\sigma_{ij})$:

$$F(\sigma_{ij}) = \bar{\tau} - c_{DP} + \mu_{DP}\sigma_{kk}/3, \tag{1}$$

where $\bar{\tau} = \sqrt{s_{ij}s_{ij}/2}$ is the second invariant of the deviatoric stress tensor $s_{ij} = \sigma_{ij} - (\sigma_{kk}/3)\delta_{ij}$, c_{DP} is related to the cohesion, and μ_{DP} is related to the internal coefficient of friction. When $F(\sigma_{ij})$ is negative, the material behaves elastically (Fig. 2). Since the material close to the fault is already damaged [*Chester and Logan*, 1986; *Chester et al.*, 1993, 2004; *Biegel and Sammis*, 2004; *Caine et al.*, 1996], we do not consider any cohesion for the off-fault material. Hence the above equation reduces to

$$F(\sigma_{ij}) = \bar{\tau} + \mu_{DP}\sigma_{kk}/3. \tag{2}$$

Our study does not consider the effects of pore fluids, but the effect of fluid pressure can be introduced into this equation by considering the stresses in the above equation as effective stresses for a fluid-saturated medium [*Dunham et al.*, 2011a; *Viesca et al.*, 2008].

For viscoplasticity, the stresses are allowed to exceed the yield function according to

$$F(\sigma_{ij}) = \Lambda\eta, \tag{3}$$

where $\Lambda = \sqrt{2\dot{e}^{pl}_{ij}\dot{e}^{pl}_{ij}}$ is the equivalent plastic strain rate from the deviatoric plastic strain rate $\dot{e}^{pl}_{ij} = \dot{\epsilon}^{pl}_{ij} - (\dot{\epsilon}^{pl}_{kk}/3)\delta_{ij}$ and η is a viscoplastic viscosity defining the time scale over which stresses can exceed the yield stress. If stresses are accumulated at a rate faster than the relaxation time of the viscoplastic material, the material behaves elastically, and the stress decays towards the yield surface over the relaxation time if no further stresses are applied. The rate-independent Drucker-Prager plasticity ($\eta = 0$) has an issue of ill-posedness under conditions permitting shear localization, but the addition of viscous relaxation creates a problem that is well-posed mathematically [*Loret and Prevost*, 1990; *Perzyna*, 1966; *Sluys and De Borst*, 1992].

The components of plastic flow are determined by

$$\dot{\epsilon}_{ij}^{pl} = \Lambda P_{ij}\left(\sigma_{ij}\right), \tag{4}$$

with $P_{ij}(\sigma_{ij}) = s_{ij}/(2\bar{\sigma}) + (\beta/3)\delta_{ij}$, where the β parameter determines the ratio of volumetric to plastic strain.

3. Fault roughness

Recent studies of fault surface topography measurements [*Sagy et al.*, 2007; *Renard et al.*, 2006; *Brodsky et al.*, 2011; *Candela et al.*, 2012, 2009, 2011] suggest that fault surfaces are self-affine fractals. A few other studies [*Brown and Scholz*, 1985; *Power and Tullis*, 1995; *Lee and Bruhn*, 1996; *Shi and Day*, 2013] suggest that fault surfaces are better described by a type of self-affine fractals that are self similar fractals. A self-affine fractal profile is one that requires a separate length and height scaling to obtain a similar statistical profile, while a self-similar fractal profile requires same length and height scaling [*Russ*, 1994]. A self-affine fault profile can be described by two parameters. The first parameter is called the Hurst exponent which quantifies the fractal scaling of the power spectrum of the fault. We denote this parameter by H. The second parameter quantifies the maximum roughness amplitude of a fractal fault profile, which we quantify through the RMS deviation of the fault profile from planarity. This parameter is dependent on the maturity of the fault. A detailed description of the self-affinity and the two parameters can be found in the appendix of our previous study [*Aslam and Daub*, 2018].

We run all of our simulations in this study on an immature self-similar fault profile. A self-similar fractal fault profile is described by $H = 1$. We describe the immaturity of the fault profile by an RMS height value of 0.01 [*Brodsky et al.*, 2011]. We run 500 spontaneous earthquake rupture simulations, each with a different realization of the immature self-similar fault profile (RMS height = 0.01 and $H = 1$) . We use a Fourier method to generate the fault profiles [*Andrews and Barall*, 2011], and cut off the fractals at a wavelength corresponding to 20 times the grid spacing. Figure 1(a) shows a self-similar fractal fault profile with RMS height of 0.01, while the variation in the shear and normal traction due to the fault profile is shown in Fig. 1(b). The plot of the shear and normal components shows that the geometry of the fault profile causes the tractions to be highly non-uniform, which subsequently alters the slip distribution of the fault when it fails.

4. Model setup

We use a plane strain model to run all of our spontaneous earthquake rupture simulations. Figure 3 shows a schematic of the model setup. The simulation domain is 130 km long and 70 km wide. The fault surface has the same length as the domain length. The fault profile is a self-similar fractal curve $f(x)$ deviating from $y = 0$ with RMS height to wavelength ratio of 0.01. We run 500 earthquake rupture simulations each with a different fault surface realization. We do this by changing the fault profile in each simulation, but keeping the rest of the modeling setup the same. We use a fixed grid spacing ($\Delta x = 25$) along strike in all of our simulations. We have run a few simulations with shorter grid spacing in our previous study and determined that the simulations are well resolved at our selected resolution. The minimum resolvable wavelength of fault roughness is 0.5 km based on our selected grid spacing ($\lambda_{min} = 20\Delta x = 0.5$ km). All of our simulations assume Drucker-Prager plastic off-fault material properties. The plastic parameter values used in this study are given in Table 1. We use `fdfault` to run all of our rupture simulations. This code has been verified on multiple SCEC benchmark problems [*Harris et al.*, 2009, 2018] both with elastic and plastic off-fault material properties.

We assume a uniform regional stress field over the whole domain. An important point to note is that when the uniform stress field is resolved on each point along the fault, it provides heterogeneous values of normal and shear traction (due to geometry of the fault profile) on the fault. As an example, Fig. 1(b) shows the traction values resolved on the fault profile (shown in Fig. 1(a)) due to the uniform stress field given in Table 1. In this study, we represent compressive stresses as negative. We do not encounter any tensile normal traction in our simulations with plastic off-fault material properties.

We use the linear slip weakening (SW) friction law to model friction on the fault [*Ida*, 1972; *Andrews*, 1976, 1985; *Day*, 1982]. According to this model, a static friction value μ_s drops to a dynamic friction value μ_d as a function of slip U on the fault over a certain critical slip distance D_c. Although this friction law has a simple formulation [*Bizzarri*, 2010], it captures the basic weakening characteristics of the friction on the fault and hence has been used in many rupture simulation studies (e.g. [*Harris et al.*, 2009]). This law does not include any healing to friction with time, hence some rupture simulation studies (e.g. [*Okubo*, 1989; *Dunham et al.*, 2011b, a; *Schmitt et al.*, 2015; *Bizzarri and Cocco*, 2006a, b]) have used other friction laws such as rate and state friction [*Dieterich*, 1979; *Ruina*, 1983] or the Shear Transformation Zone friction law [*Daub and Carlson*, 2010] to account for the fault friction properties. We choose $\mu_s = 0.7$, $\mu_d = 0.2$ and $D_c = 0.4$ m in this study. A low value of dynamic friction with a higher strength is chosen based on lab experiments [*Goldsby and Tullis*, 2011, 2002; *Hirose and Bystricky*, 2007; *Di Toro et al.*, 2011, 2004; *Hirose and Shimamoto*, 2005; *Tsutsumi and Shimamoto*, 1997; *Beeler et al.*, 2008; *Han et al.*, 2007] and theoretical/numerical studies [*Bizzarri*, 2011; *Andrews*, 2002; *Suzuki and Yamashita*, 2006; *Rice*, 2006; *Beeler et al.*, 2008] to provide strong dynamic weakening. Our static friction value for the SW law remains constant but at any time snapshot the friction on the fault is variable along the fault due to the heterogeneous distribution of fault slip.

Studies of dynamic rupture simulations show that the plastic strain accumulation occurs predominantly on the extensional side of the fault [*Templeton and Rice*, 2008; *Ben-Zion and Shi*, 2005]. The extensional side can be defined by the sign of the fault parallel component of the strain tensor (ϵ_{xx}) near the rupture front [*Templeton and Rice*, 2008]. The static stress changes induced by co-seismic slip on the fault during rupture propagation vary in space, with a dependence on whether the point is located on the compressional or extensional side of the fault. Since our main focus in this study is to calculate static stress changes as a result of earthquake rupture, we aim to compare the static stress changes on both the extensional and compressional sides of the fault. To make this comparison more straightforward, we run a unilateral rupture in all of our rupture simulations. Doing this enables the compression to be dominant along one side of the fault and extension to be dominant along the other side of the fault. We choose the right side of the fault (a 3 km nucleation patch between $80 - 120$ km along fault distance) to initiate slip in all of our rupture simulations. To pick the exact location of 3 km nucleation patch between the along fault distance $80 - 120$ km, we calculate the shear to normal stress ratio (S/N ratio) at every grid point along the fault and choose the location where the S/N ratio is highest. These locations are the places where ruptures are more likely to nucleate [*Fang and Dunham*, 2013; *Oglesby and Mai*, 2012; *Mai et al.*, 2005]. Since every fault profile does not fulfill this criteria, we generate a large number of fault profiles and calculate the S/N ratio of each of these fault profiles. If the S/N ratio is highest between $80-120$ km along fault distance, we keep this fault profile for rupture simulation; otherwise we discard the fault profile. To force the rupture to propagate only towards the left side of the fault, we place a frictional barrier on the right side of the fault. The frictional barrier length starts from the right edge of the nucleation zone and ends at the right fault edge as can be seen in Fig. 3. We select 500 different fault profiles using the above criteria and run simulations on those fault profiles. After running the simulations, 187 ruptures propagate more than 60 km from the nucleation point before dying out, while the rupture in the remaining simulations die out early due to the unfavorable fault geometry. For our results section, we only consider those 187 ruptures that have ruptured at least 60 km along strike.

Previous researchers have used many strategies to spontaneously nucleate a rupture for the SW friction law [*Day*, 1982; *Bizzarri and Cocco*, 2005; *Dunham and Archuleta*, 2005; *Ionescu and Campillo*, 1999; *Andrews*, 1985]. Strategies that are commonly used include time independent over-stressing of the fault (e.g. [*Harris et al.*, 2009]) and over-stressing a single node point within a critically stressed nucleation patch (e.g. [*Schmedes et al.*, 2010]). We choose the time independent over-stressing of the fault nucleation patch based on our analysis of different nucleation strategies in our previous study. The fault nucleation patch is 3 km wide while the central point of the patch is the point with the highest S/N ratio. The shear traction on each point of this nucleation patch is increased from its current value to a value defined by the failure stress on the fault: $T_s^{(i)} = 1.01T_f^{(i)} =$

$\mu_s T_n^{(i)}$, where ${T_s}^{(i)}$ is the shear traction, ${T_f}^{(i)}$ is the failure traction and ${T_n}^{(i)}$ is the normal traction on the ith point on the fault.

5. Receiver fault orientations and potential aftershock zone calculations

The static stress change on a receiver fault is calculated using the CFF equation. The CFF is based on the change in the normal and shear stress on a receiver fault [*King et al.*, 1994]:

$$\Delta\sigma_\beta^f = \Delta\tau_\beta - \mu_\beta \Delta\sigma_\beta. \tag{5}$$

Here $\Delta\sigma_\beta^f$ is the Coulomb stress change, $\Delta\tau_\beta$ is the shear stress change, μ_β is the friction coefficient and $\Delta\sigma_\beta$ is the normal stress change on the receiver fault. The subscript β specifies that all the stress values are calculated on the receiver fault plane (i.e. τ_β and σ_β are calculated by resolving the off-fault stresses onto the receiver fault plane). An increase in the CFF value moves the fault closer to the failure, while a decrease in the CFF value moves the fault away from failure.

Since the dynamic rupture simulations solve for the stresses directly during slip, we have the complete stress tensor available at the end of the simulation. Once we know the receiver fault orientation, we can calculate the static stress change on the receiver fault. We assume a frictional coefficient value (μ_β) of 0.4, a value typical for strike-slip receiver faults [*Parsons et al.*, 1999].

We treat the compression and extensional sides separately when calculating CFF values. We calculate CFF values on the compressional side of the fault using a single receiver fault orientation. This orientation is parallel to the overall trace of the host fault. The assumption of parallel receiver faults is usually reasonable for strike slip fault zones [*Faulkner* *et al.*, 2003]. We calculate CFF values on the extensional side of the fault using the fault parallel receiver fault orientation (similar to the compressional side), and also using a second receiver fault orientation that is spatially variable. We determine this second orientation of the receiver fault using the final plastic strain tensor of dynamic rupture simulation. Using this tensor, we calculate the orientation at which the plastic shear strain is maximum, which should serve as a proxy for the likely orientation of faults in that area due to off-fault damage.

We extract the plastic strain and final stress tensor after a sufficiently long simulation time to ensure that our calculation of the static stress change is not affected by the dynamic stresses due to passing seismic waves. We also select a smaller domain of the model to extract the stress and plastic strain tensor rather the full domain which further reduces the effects of boundaries and dynamic waves. We extract both tensors after 41.13 sec of rupture simulation. Based on the shear wave velocity, this time is sufficient for the waves to propagate away from the central part of the modeling domain. The smaller domain is 50 km long and 40 km wide, beginning at 20 km along fault distance and ending at 70 km along fault distance for fault parallel direction while starting at -20 km and ending at 20 km across fault distance for the fault perpendicular direction as can be seen in Fig. 4. The dashed vertical lines shows the sub-region along fault strike that is used for analysis.

Once we calculate the CFF on both sides of the fault from all of the simulations, we compute point statistics by combining the calculated CFF values from each realization. We also analyze the spatial and amplitude correlations of these CFF values. We do this by identifying the zones of positive CFF change on each side of the main fault for all 187 simulations and then calculate the size, location and mean CFF amplitude of each zone. We only consider positive CFF zones that has a length of 100 m or more. In addition to the size and location of these zones, we calculate the total number of these positive CFF zones that exist within the selected sub-domain in each realization on each side of the fault. This comparison illustrates how static stress changes (due to co-seimic fault slip) are distributed on the compressional and extensional sides of the fault.

To compare our model results with real aftershock data as described in the following section, we find the distance of each positive CFF zone from the host fault and its area from each simulation. We determine the area of each positive CFF zone by calculating its length and then convert it to area by assuming that this zone hosts a circular rupture patch. The assumption of a circular rupture is frequently used for small to moderate earthquakes [*Aki*, 1972; *Thatcher and Hanks*, 1973; *Hanks*, 1977; *Scholz*, 1982; *Allmann and Shearer*, 2009]. By calculating the areas of all positive CFF zones for both the compressional and extensional side in each simulation, we obtain a statistical ensemble of the maximum possible rupture area and its distance from the main fault for many ruptures.

6. Aftershocks and fault trace data

To compare our model results with real data, we select five major earthquakes in California. These events include the Morgan Hill Earthquake of 1984 with moment magnitude (M_w) = 6.2 [*Beroza and Spudich*, 1988], the Loma Prieta Earthquake of 1989 with $M_w = 6.9$ [*Wald et al.*, 1991], the Landers Earthquake of 1992 with $M_w = 7.2$ [*Wald and Heaton*, 1994], the Northridge Earthquake of 1994 with $M_w = 6.2$ [*Hartzell et al.*, 1996], and the Hector Mine Earthquake of 1999 with $M_w = 7.1$ [*Salichon et al.*, 2004]. We use the relocated Northern and Southern California earthquake catalog [*Shearer et al.*, 2005; *Waldhauser and Schaff*, 2008] to extract the aftershocks related with the earthquakes described above. We keep a fixed time window after the main shock to extract aftershocks. Previous works have used a magnitude-dependent time window to determine aftershocks [*Gardner and Knopoff*, 1974; *Allen et al.*, 1965]; however, we use a fixed time window to ensure uniform treatment of all events. We extract the fault trace of all the earthquakes described above using the slip inversion of these earthquakes. The slip inversions are freely available through an online database (SRCMOD) [*Mai and Thingbaijam*, 2014]. This database has the record of the estimated slip model for many major earthquakes around the globe through finite fault inversion studies.

To perform a quantitative comparison of the observational data with our model results, we calculate the earthquake rupture area of all aftershocks from the five major earthquakes described above using the standard Eshelby formula [*Eshelby*, 1957] which assumes a circular source dimension and a constant stress drop value. We assume a stress drop of 1 MPa which is typical for geometrically heterogeneous faults [*Bailey and Ben-Zion*, 2009; *Shaw et al.*, 2015].

7. Results

7.1. point statistics

Figure 4(a) shows the pattern of off-fault plastic deformation during one of the rupture simulations. The pattern of off-fault plastic deformation is shown using the equivalent plastic strain γ^p, defined as $\Lambda = \frac{d\gamma^p}{dt}$. The plastic strain accumulates along the extensional side of the fault as observed in many other studies [*Templeton and Rice*, 2008; *Ben-Zion and Shi*, 2005; *Andrews*, 2005] with the width of plastic deformation zone increasing with the rupture propagation distance. The roughness of the fault profile concentrates the regions of highest plastic strain immediately next to the geometrical fault bends. These high strain zones tend to be localized in space due to stress concentrations as shown in Fig. 4(a). Some of these localized higher plastic strain zones are marked in Fig. 4(a) by ‘A’, ‘B’ and ‘C’. The restraining bends of the fault geometry makes it difficult for the rupture to break through, causing stress concentration nearby. These localized zones of plastic strain have been observed by previous dynamic rupture studies performed on geometrically complex rough faults [*Dunham et al.*, 2011a; *Johri et al.*, 2014]. Figure 4(b) shows the estimated receiver fault orientations using the direction of maximum plastic shear strain. The orientations vary between 0°-45° from the overall trace of the main fault. The receiver fault orientations are mostly within 20° of the main rupture trace. The dashed vertical line shows the sub-region from which the stress and plastic strain values are extracted for further static stress calculation.

Figure 5 shows the change in stresses (normal and shear) for the sub-region marked in Fig. 4. As can be seen in Fig. 5, the stresses are highly complex in the region near the fault. The geometric heterogeneity of the fault profile leads to this complexity in the stress distribution. Farther from the fault profile, the stress complexity is reduced as the fault roughness effects are not as prevalent at those distances. Furthermore, though the stresses are highly complex, we note from Fig. 5(b) that the negative shear stress change values dominate the positive values of stress change. Similar to our previous study [*Aslam and Daub*, 2018], we divide the region across the fault into three sub-regions based on the stress pattern. We refer the region close to the fault where the stresses are more complex as the the ‘near-fault’ region, while we refer the region of relatively uniform stresses as the 'far-fault' region. We refer the transition region between the near-fault region and the far-fault region as the intermediate region. Most of our discussion of results in this study is related to the near-fault region since this region is mainly affected by the fault roughness during rupture propagation. Both the near-fault region and the far-fault region are marked in Fig. 5. We note that this naming convention is only for the purpose of discussing the results in this study; on tectonic scales, both of these regions are close to the fault.

Using the final stress tensor from each of the rupture simulations, we calculate the CFF in the region surrounding the main fault. To calculate the CFF values, we use two different receiver fault orientation approaches. In the first approach, we assume parallel receiver fault orientations, while in the second approach, we calculate CFF values based on the receiver fault orientations calculated from the direction of maximum plastic shear strain. Since no plastic strain accumulates on the compressional side of the fault profile, we only calculate the CFF using the second approach for the extensional side of the fault. Figure 6 shows the CFF calculated using the parallel receiver fault orientation on both the compressional and extensional sides of the fault. Similar to the distribution of stresses shown in Fig. 5, the CFF distribution is also highly complex across the fault in the near-fault region with both negative and positive CFF change zones present in this region. At distances farther from the near-fault region, the CFF change pattern is more uniform, with negative CFF values dominating. Based on the realization shown in Fig. 6, there is not an obvious difference between the extensional and compressional sides of the fault. Therefore, we examine a statistical ensemble of all CFF values from both the extensional and compressional sides of the fault in addition to examining each side separately. The regions of positive CFF change in Fig. 6 are of particular importance, as these are the regions which are brought closer to failure and are potential locations of aftershocks. We note from Fig. 6 that the roughness of the fault profile causes many small positive CFF zones to occur within broader negative CFF zones. These small positive CFF zones are not resolvable using the usual CFF calculations due to coarser resolution of fault slip from the inversion studies, and hence these zones would appear as stress shadows. At far-fault distances, where the fault roughness effects are not present, we do not see these positive CFF zones.

We mark the boundaries between the near-fault, intermediate, and far-fault regions based on the number of positive CFF zones. In this study, we consider a region to be a positive CFF zone if it has a length of at least 100 m (i.e. at least 4 consecutive positive CFF values along the direction of the receiver fault orientation). In each simulation, we first count the total number of positive CFF zones at each distance away from the trace of the main fault and then include distances with more than 8 positive CFF zones in the near-fault region. The distance at which the number of positive zones decreases from > 8 to ≤ 8 marks the boundary between the near-fault region and the intermediate region. The distance where no positive zones are observed designates the start of the far-fault region. We calculate the width of the near-fault region for both the compressional and the extensional side from each rupture simulation. The width of the near-fault region describes the distance over which the stress complexity as well as the damage pattern complexity may influence seismicity patterns. The average width of the near-fault region is 1890 m on the extensional side when CFF values are calculated using parallel receiver fault orientations, 2730 m when the CFF values are calculated using variable receiver fault orientations, and 1680 m on the compressional side of the fault.

We combine the CFF data from each side (both extensional and compressional) for all 187 rupture simulations to examine the statistical properties of the CFF as a function of distance. Figure 7 shows the probability density function (PDF) values of the CFF as a function of distance from the fault. Figure 7(a) shows the PDF of the CFF for the compressional side, Fig. 7(b) shows the PDF of the CFF for the extensional side, and Fig. 7(c) shows the PDF of the CFF by combining CFF values from the extensional and compressional side. It is important to note that Figs. 7(a), 7(b) and 7(c) are constructed using parallel receiver fault orientations. Figure 7(d) shows the PDF of the CFF as a function of distance where the CFF is calculated using variable receiver fault orientations. In each of the plots in Fig. 7, the general behavior of the CFF values with distance from the fault remains the same. The regions close to the fault show a wider spread of CFF values, and as the distance from the fault increases, this spread gradually squeezes to a relatively narrow band of values. The distance at which we begin observing a narrow band of values of the CFF marks the transitional boundary between the near-fault region and the intermediate/far-fault region. The spread of the CFF values in the intermediate/far-fault region is not as narrow as is observed when running the same simulations with off-fault elastic properties [*Aslam and Daub*, 2018] (the figure showing the PDF of the CFF calculated assuming off-fault elastic response is provided in the supplementary material). This may be related to the fact that the off-fault stresses are smoothed when considering off-fault plasticity. Furthermore, We note from Fig. 7 that the range of values in the intermediate/far-fault region remains the same for simulations with elastic material properties but fluctuates between different upper and lower CFF bounds for the case of simulations with plastic off-fault material properties. When comparing the CFF values between the extensional side (Fig. 7(b) and 7(d)) and the compressional side (Fig. 7(a)) for the intermediate/far-fault region, we observe that the compressional side has more sharp fluctuations between different upper and lower CFF bounds, as no damage occurs on that side of the fault. In Fig. 7(d), the optimum orientations of the receiver faults change mainly the extreme CFF values with the largest and smallest CFF values. This is the reason that the difference between Fig. 7(b) and Fig. 7(d) is not obvious by eye. However, this change in the extreme values of the CFF does influence the locations of aftershocks, which we investigate through the spatial correlations of the CFF function.

7.2. Spatial correlations

All of our results described above are based on one point statistics from our simulations. Although one point statistics provide many useful insights into the static stresses, aftershocks are not point features, but spatially extended events that rupture an area that depends upon the magnitude of the aftershock. To study this, we extract information related to the spatial correlations in the positive CFF values. To do this, we use the locations as well as lengths of positive CFF zones. To calculate the length of a positive CFF zone, we first pick a point at any distance away from the fault and then find the orientation of the receiver fault at that point (0° for the case of parallel receiver fault orientations and a spatially-dependent value for the case of variable receiver fault orientations). We then calculate the CFF value at that point, if the CFF value is positive, we move 25 m further along the direction of the receiver fault orientation and calculate the CFF value at the next point. If this point is not on a grid point, we calculate its CFF value by interpolating the stress values at this point. We use linear interpolation [*Barber et al.*, 1996] to compute the stress values at points which do not lie on the simulation grid. We continue along the same direction and increase the length of the positive zone until we encounter a negative CFF value. Figure 8 shows the total number of positive CFF zones in each rupture simulation at two different distances from the main fault on the extensional side of the fault. Figure 8(a) shows the number of positive CFF zones 100 m from the fault, while Fig. 8(b) shows the number of positive CFF zones 3.5 km from fault. We observe that the number of positive zones decreases as the distance from the fault increases. This is because at greater distances, the fault roughness effects are less prevalent, as is evident from Figs. 5 and 6. This behavior remains the same irrespective of the methodology used to calculate the positive CFF zones (i.e. either CFF calculated using a parallel receiver fault orientation or calculated using a variable receiver fault orientation). In the near-fault region, we observe twice the number of positive CFF zones for the variable off-fault orientations case when compared to the parallel receiver fault orientations (Fig. 8(b)). This is because when calculating CFF assuming variable receiver fault orientations, the directions that have minimum compressive normal stress and maximum shear stress are favored. This causes many more locations to have a positive CFF value than those found using a parallel receiver fault orientation. An increase in the number of positive CFF zones for the case of variable receiver fault orientations means an increase in the width of the near-fault region. This indicates that the fault roughness effects are observed at greater distances when off-fault material damage and dynamic calculations of receiver fault orientations are considered. The comparison between the number of positive CFF zones with the two types of receiver fault orientations suggests that the calculations of dynamic off-fault orientations are important at distances close to the fault since they can significantly affect the spatial location and magnitude of aftershocks. Furthermore, comparing Figs. 8(a) and 8(b), we can see that the orientations derived from the damage zone are clearly well aligned with the stress field in the near-fault region, and they lead to a greater variability in the number of zones in the intermediate region.

Since we have calculated the locations and rupture lengths of the positive CFF zones surrounding the main fault in each simulation, we can combine this information from each simulation to examine the spatial characteristics of probable aftershock zones surrounding a complex fault. To estimate the maximum possible magnitude of each of the calculated positive zones, we assume that each patch hosts a circular patch rupture and convert that area into a magnitude using standard scaling relations. Figure 9 shows the plot of joint PDF of rupture areas as a function of distance for all probable aftershock zones. The plot combines all the positive CFF zone data from each simulation. The plots shows both smaller rupture zones with small rupture areas (< 2.5 km^2) and larger rupture zones with larger rupture areas (> 2.5 km^2) are present at all distances from the fault. The smaller rupture zones have a higher probability of occurrence at distances closer to the near-fault region than the larger rupture zones. This behavior is observed independent of the choice of receiver fault orientation. For distances within the intermediate zone, we observe smaller and larger rupture zones to have a similar probability of occurrence. This behavior remains the same for calculations using both parallel and variable receiver fault orientations. When comparing Figs. 9(a) and 9(b), we see that the higher probabilities for smaller rupture zones in the near-fault region are more uniformly distributed with distance when calculated using variable off-fault orientations as compared to rupture zones calculated using parallel receiver fault orientations. This is due to the fact that there are a higher number of smaller zones calculated using variable off-fault orientations than for the case of parallel fault orientations. We observe no larger ruptures (with rupture areas > 1 km^2) for distances less than 200 m in Fig. 9(a) when compared to Fig. 9(b), and fewer smaller ruptures (with rupture area < 0.1 km^2) for distances greater than 4 km. Figure 9(b) is more complete in terms of probable rupture areas (fewer white spaces with PDF value $= 0$) because we observe many more rupture zones with a range of areas calculated using variable receiver fault orientations. These rupture zones are distributed throughout the near-fault and intermediate regions surrounding the main fault and fill in the empty portions of Fig. 9(b). Since the region closer to the fault is highly damaged [*Faulkner et al.*, 2011], and the stresses in this region are complex [*Erlingsson and Einarsson*, 1989; *Aslam and Daub*, 2018; *Pedersen et al.*, 2003], we expect real aftershocks to have a range of rupture lengths giving rise to behavior that is similar to what we observe in Fig. 9(b).

Our modeling suggests a greater probability of occurrence of smaller area rupture zones in the near-fault region as compared to the intermediate region. There may also be a correlation between positive CFF zone areas and the mean amplitude of stress increase. To examine this, we calculate the mean CFF amplitude for each rupture zone. Figure 10 shows the amplitude of CFF as a function of rupture area from all of our simulations. Figures 10(a)-(c) show rupture zones calculated using parallel receiver fault orientations while Figs. 10(d)-(f) are based on calculations using variable receiver fault orientations. It is evident in Figs. 10(a) and 10(d) that the mean CFF amplitude decays with distance and with increasing zone area. Similarly, it can be clearly observed from Figs. 10(c) and 10(f) that the rupture zones are mostly smaller in the near-fault region and have higher CFF amplitudes, while the CFF amplitudes are smaller at intermediate distances for both smaller and larger zones (Figs. 10(b) and 10(e)). Based on the comparison of CFF amplitudes in the near-fault region (Figs. 10(c) and 10(f)), we find that the CFF amplitudes calculated using variable receiver off-fault orientations are relatively low when compared to CFF amplitudes calculated using parallel off-fault receiver orientations. Similarly, the CFF amplitudes have a greater spread in Fig. 10(c) as compared to Fig. 10(f). This is because the optimum orientations of the receiver fault tend to smooth the CFF values, and increases the connectivity between positive zones, as plastic deformation tends to remove extreme stress values from the distribution.

7.3. Real data comparison

To compare our modeling results with real observations, we compile a dataset by considering aftershocks from five major earthquakes in California. Figure 11(a) shows the trace of the rupture of 1999 Hector Mine earthquake. The induced CFF change in the surrounding region due to this earthquake, at the focal depth of 7.5 km, is calculated and plotted in Fig. 11(a). The CFF change is calculated using the slip model of *Salichon et al.* [2004]. We see a prominent stress shadow in the center of the fault with two positive CFF zones around the fault in the near-fault region. Figure 11(b) shows the magnitude-frequency distribution of all the aftershocks from the compiled dataset. We note that the magnitudes of the aftershocks follow the Gutenberg-Richter magnitude-frequency (GR) distribution [*Gutenberg and Richter*, 1944]. To construct Fig. 11(b), We only pick those aftershocks that are located in the region $<$ 5 km away from the fault rupture to compare them with our near-field model results. To determine how the rupture areas of these aftershocks depend on distance, we calculate the joint PDF values of the rupture areas and distances from the fault for the aftershocks of five major earthquakes. It is important to note that Fig. 11(c) shows the same information as Fig. 9, but it illustrates the joint PDF for aftershocks rather than the positive CFF zone areas from our models. The data shown in in Fig. 11(c) presents similar behavior to what is observed from our modeling results. Rupture zones with all rupture areas (i.e. both smaller (< 0.45 km^2) and larger (≥ 0.45 km^2)) are present in both the near-fault and intermediate regions. Similar to our modeling results, the smaller rupture areas are relatively more probable than the larger rupture areas in the near-fault region. In the intermediate region, we see a relatively high probability of smaller rupture lengths when compared to the larger rupture lengths. Since our model does not add any constraints on the existence of smaller size events within the larger CFF zone, the additional events with small rupture areas at all distances in the observations are likely due to events that do not fill the entire positive CFF zone. A comparison of the histograms of aftershock distances from the fault plane for $M_w > 2$ and $M_w > 3$ (Fig. 11(d)) shows that the aftershocks follow a GR distribution at all distances. Based on our model results, we suggest that this arises possibly due to the roughness of the fault which produces positive CFF change zones of a variety of different areas at all distances in the near-fault region. Hence, these positive CFF zones are likely to host some smaller events, resulting in the GR distribution at all distances.

8. Discussion

In this work, we perform dynamic rupture simulations with off-fault plasticity on rough strike slip faults to investigate the occurrence of aftershocks in the near-fault region and in the region of stress shadows [*Segou and Parsons*, 2014; *Kilb et al.*, 1997; *Beroza and Zoback*, 1993]. We perform rupture simulations on many realization of a self-similar rough fault profile with RMS height of 0.01. We calculate the CFF values on the extensional side using variable and parallel receiver fault orientations. We use plastic strain accumulation [*Templeton and Rice*, 2008; *Ben-Zion and Shi*, 2005; *Andrews*, 2005] to calculate the variable orientations of receiver faults. The pattern of static stress change is highly complex [*Chester and Chester*, 2000; *Dieterich and Smith*, 2009] in the near-fault region irrespective of which approach is used to calculate the CFF value. Similarly, our calculations suggest that the PDF of the CFF distribution follows a pattern where a large spread of the CFF values in the near-fault region collapses to a narrow CFF spread at intermediate and far-fault distances.

We extract the spatial correlation characteristics of the positive CFF values from our model results. In particular, we are interested in the spatial extent of positive CFF zones since these are potential locations of future aftershocks. We find many small positive CFF zones to be present within larger negative CFF zones. These smaller positive CFF zones which are not resolvable using the usual CFF calculations would appear as stress shadows in observational studies [*Freed*, 2005; *Segou and Parsons*, 2014]. Our calculations show that, in the near-fault region, the positive CFF zones are twice as probable in the near-fault region when CFF values are calculated using variable off-fault orientations in comparison to CFF values calculated using parallel receiver fault orientations. An increase in the number of positive CFF zones causes an increase in the width of the near-fault region for the case of variable receiver fault orientations. This suggests that off-fault material damage tends to affect the spatial characteristics and decay of aftershocks with distance. Furthermore, if many more positive zones at close distances are present within a certain region, there is a higher probability that the rupture on these small zones can propagate through the zone of negative CFF values between them and grow into a larger rupture. This suggests that the off-fault damage [*Chester and Logan*, 1986; *Myers and Aydin*, 2004; *Faulkner et al.*, 2011; *Chester et al.*, 1993, 2004; *Biegel and Sammis*, 2004; *Caine et al.*, 1996] is important along with the observed stress complexity of the fault system [*Erlingsson and Einarsson*, 1989; *Pedersen et al.*, 2003] in order to determine the locations and magnitudes of aftershocks in a particular region.

Most of the aftershocks occur in the immediate vicinity of a large fault [*King et al.*, 1994; *Stein et al.*, 1994; *Freed*, 2005; *Liu et al.*, 2003]. The material in this region is much weaker than the adjacent country rock [*Faulkner et al.*, 2003; *Cochran et al.*, 2009; *Hauksson*, 2011, 2010]. The weaker zone is due to the complex damage in the near-fault region that has been observed by many observational studies [*Faulkner et al.*, 2010, 2011; *Myers and Aydin*, 2004; *Andrews*, 2004, 2005; *Rice et al.*, 2005]. This highly damaged weak zone influences the spatial seismicity distribution [*Hauksson*, 2011, 2010]. Some studies (e.g. [*Liu et al.*, 2003; *Powers and Jordan*, 2010]) were carried out to estimate the size of the damage zone surrounding a large fault using aftershock data. In this study, we examine if the decay of seismicity with distance from the fault is controlled only by the stress field decay or if the damage zone also influences the decay of seismicity. Our comparison of amplitudes of CFF as a function of areas and distances (Fig. 10) suggests that both the stress field decay and the damage zone complexity affect the decay of seismicity with distance. The stress field fluctuations decay with distance, but the damage zone plays a role by aligning fault orientations with the optimal stress orientations for failure. This is particularly obvious from the outlier values seen in Fig. 10 (d) and (e), which do not follow the usual trend of the amplitude as a function of distance seen in Fig. 10(a), suggesting that the damage zone complexity cannot be neglected when examining seismicity patterns near active faults.

Many quasi-static modeling studies have examined static stress changes and the consequent aftershock distribution in the near-fault region as a result of slip on rough faults. *Shaw et al.* [2015] considered a multi-strand fault system to run their quasi-static model and found that the reduced ground motion amplitudes of aftershocks occurred in the near-fault regions are predominantly due to smaller stress drop of these events. Their model was able to capture many of the characteristics of spatial and temporal clustering of aftershocks. *Smith and Dieterich* [2010] also considered a rough fault to perform quasi-static modeling and showed the occurrence of aftershocks in small positive CFF zones within stress shadows. *Powers and Jordan* [2010] used the quasi-static model of *Dieterich and Smith* [2009] to constrain the width of the near-fault region for different faults in California. Though the quasi-static models of fault slip on rough faults were able to explain some of the important characteristics of aftershock distribution, these calculations were solely based on stresses since these models lack any physical representation of likely orientations of receiver faults in the damage zone. Our dynamic earthquake rupture simulation study can provide constraints on the characteristics of damage zone that may be included into the quasi-static models to get improved estimates of the spatial distribution of aftershocks in a self-consistent manner.

A focal mechanism solution provides the information of slip direction and fault-plane orientation of an earthquake through its radiation pattern [*Hardebeck and Shearer*, 2002]. This information is then used to derive the orientation of stresses causing the earthquake (e.g. [*Mallman and Parsons*, 2008; *Hardebeck*, 2015; *Beroza and Zoback*, 1993; *Hardebeck*, 2010]. In many cases, the focal mechanisms are diverse in the near-fault region [*Beroza and Zoback*, 1993; *Bailey et al.*, 2010; *Smith and Heaton*, 2011] and do not align, suggesting a complete stress drop in order to produce the variable orientations of aftershocks. This was the case for orientations observed by *Kilb et al.* [1997] from earthquakes following the 1989 Loma Prieta earthquake. However, some studies show good alignment of focal mechanisms of aftershocks with the mainshock [*Michele et al.*, 2016]. We see that our receiver fault orientations are predominantly within the "acceptable" range of the *Kilb et al.* [1997] study, suggesting that the dynamic rupture studies can be used to infer the likely orientations of receiver faults in the damage zone.

All of our simulations are performed in 2D. A real earthquake does not occur in 2D but rather occurs in 3D on a 2D fault. In 3D ruptures, the process of rupture propagation may change if the rupture in the third direction is not coherent [*Dunham et al.*, 2011a; *Shi and Day*, 2013]. This may also cause some differences in the pattern of stress change in the off-fault region. Furthermore, we use the plastic strain accumulation during rupture propagation to calculate receiver fault orientations. This approach only accounts for the faults that are created during the dynamic rupture events. This may not always be the case as the receiver faults may also be pre-existing and have an orientation that is unrelated to the present tectonic behavior [*Toda et al.*, 2008; *Lin and Stein*, 2004; *Toda et al.*, 2005; *Tse and Rice*, 1986; *Rice*, 1993; *Nielsen and Knopoff*, 1998; *Hainzl et al.*, 2010; *Lapusta et al.*, 2000; *Duan and Oglesby*, 2005; *Oglesby and Mai*, 2012]. However, if such knowledge is available from, for instance, geological mapping studies, it can easily be included in the present methodology.

Our model results are consistent with the earthquake observations. Our model suggests a higher probability of smaller rupture zones in the near-fault region as compared to larger rupture zones. This behavior is similar to the aftershock data which suggests a higher probability of smaller rupture zones in the near-fault region as compared to the larger rupture areas. One effect that we do not include is the secondary triggering caused by aftershocks [*Meier et al.*, 2014; *Marsan*, 2005; *Hanks*, 1992; *Kagan*, 1994; *Helmstetter et al.*, 2005] after one major earthquake causing the static stresses to redistribute. Our model does not capture this effect, though the secondary triggering methodology could be combined with our approach. The static stress changes can also cause pore-pressure variations if the medium is saturated with fluids. This process can affect the aftershock distribution of a region in space [*Nur and Booker*, 1972; *El Hariri et al.*, 2010; *Gupta*, 2002; *Chen et al.*, 2012] and time [*Chen et al.*, 2012; *El Hariri et al.*, 2010; *Freed*, 2005]. The aseismic slip of a fault also has the tendency to change the static stresses induced due to the co-seismic slip on the fault [*Vidale et al.*, 2006; *Vidale and Shearer*, 2006]. Constraining the role of each of these mechanisms described above is difficult [*Lohman and McGuire*, 2007; *Vidale and Shearer*, 2006; *Hainzl*, 2004; *Waite and Smith*, 2002], and it is not clear if these mechanisms may work together in a certain region to change static stresses or a single mechanism may dominate over the other mechanisms. Furthermore, other factors like topography of a region, V_p/V_s ratio of a region, heat flow and crustal thickness [*Hauksson*, 2011] of a region, and material contrasts [*Rubin and Gillard*, 2000; *Rubin and Ampuero*, 2007] across a major fault have also been observed to change the static stresses of those regions causing variations in the distribution of aftershocks. We do not model any of these phenomena in our calculations, while the observational data may include effects from these mechanisms. Overall, our findings from this modeling study are consistent with the general behavior observed in the spatial seismicity patterns. This may suggest that the supplementary mechanisms (mentioned above) are more important to include in the models when more emphasis is given to the temporal behavior of aftershocks, rather than their spatial location.

Based on our modeling results, we suggest that the damage zone is an important factor for estimating the future hazard and risk estimates of a particular region. This is because the damage zone controls the decay of aftershocks with distance together with the stress field decay with distance. A modification to the classical Coulomb failure function which considers the damage state of the near-fault region may provide a better fit to spatial aftershock distribution observed for large earthquakes as compared to classical static stress calculations. Our results suggest that knowledge of the damage zone and the likely orientations of receiver faults from physical models can provide improved constraints on the magnitude and spatial distributions of aftershock occurrence. Such methods may help improve forecasting of off-fault seismicity and improve estimates of seismic hazard in a variety of tectonic contexts.

Acknowledgments. This work was supported by the Southern California Earthquake Center (SCEC). The contribution no. is 8988. SCEC is funded by NSF Cooperative Agreement EAR-1033462 & USGS Cooperative Agreement G12AC20038. We thank the University of Memphis for providing their High Performance Computing facilities to run rupture simulations. The northern California earthquake catalog is available through weblink: http://www.ldeo.columbia.edu/∼felixw/NCAeqDD/. The southern California earthquake catalog is available through weblink: http://scedc.caltech.edu/research-

tools/alt-2011-dd-hauksson-yang-shearer.html. The rupture code used in this work is available on GitHub (URL: https://github.com/egdaub/fdfault).

References

Aki, K. (1972), Earthquake mechanism, *Tectonophysics*, *13*(1-4), 423–446.

Allen, C. R., P. St. Amand, C. Richter, and J. Nordquist (1965), Relationship between seismicity and geologic structure in the Southern California region, *Bulletin of the Seismological Society of America*, *55*(4), 753–797.

Allmann, B. P., and P. M. Shearer (2009), Global variations of stress drop for moderate to large earthquakes, *Journal of Geophysical Research: Solid Earth*, *114*(B1).

Andrews, D. (1976), Rupture propagation with finite stress in antiplane strain, *Journal of Geophysical Research*, *81*(20), 3575–3582.

Andrews, D. (1985), Dynamic plane-strain shear rupture with a slip-weakening friction law calculated by a boundary integral method, *Bulletin of the Seismological Society of America*, *75*(1), 1–21.

Andrews, D. (2002), A fault constitutive relation accounting for thermal pressurization of pore fluid, *Journal of Geophysical Research: Solid Earth*, *107*(B12), ESE–15.

Andrews, D. (2004), Rupture models with dynamically determined breakdown displacement, *Bulletin of the Seismological Society of America*, *94*(3), 769–775.

Andrews, D. (2005), Rupture dynamics with energy loss outside the slip zone, *Journal of Geophysical Research: Solid Earth*, *110*(B1).

Andrews, D., and M. Barall (2011), Specifying initial stress for dynamic heterogeneous earthquake source models, *Bulletin of the Seismological Society of America*, *101*(5), 2408–2417.

Aochi, H., E. Fukuyama, and M. Matsu'ura (2000), Selectivity of spontaneous rupture propagation on a branched fault, *Geophysical Research Letters*, *27*(22), 3635–3638.

Aslam, K. S., and E. G. Daub (2018), Effect of fault roughness on aftershock distribution: Elastic off-fault material properties, *Journal of Geophysical Research: Solid Earth*, *123*(11), 9689–9711.

Bailey, I., and Y. Ben-Zion (2009), Statistics of earthquake stress drops on a heterogeneous fault in an elastic half-space, *Bulletin of the Seismological Society of America*, *99*(3), 1786–1800.

Bailey, I. W., Y. Ben-Zion, T. W. Becker, and M. Holschneider (2010), Quantifying focal mechanism heterogeneity for fault zones in central and southern California, *Geophysical Journal International*, *183*(1), 433–450.

Barber, C. B., D. P. Dobkin, and H. Huhdanpaa (1996), The quickhull algorithm for convex hulls, *ACM Transactions on Mathematical Software (TOMS)*, *22*(4), 469–483.

Beeler, N., T. Tullis, and D. Goldsby (2008), Constitutive relationships and physical basis of fault strength due to flash heating, *Journal of Geophysical Research: Solid Earth*, *113*(B1).

Ben-Zion, Y., and Z. Shi (2005), Dynamic rupture on a material interface with spontaneous generation of plastic strain in the bulk, *Earth and Planetary Science Letters*, *236*(1-2), 486–496.

Beroza, G. C., and P. Spudich (1988), Linearized inversion for fault rupture behavior: application to the 1984 Morgan Hill, California, earthquake, *Journal of Geophysical Research: Solid Earth*, *93*(B6), 6275–6296.

Beroza, G. C., and M. D. Zoback (1993), Mechanism diversity of the Loma Prieta aftershocks and the mechanics of mainshock-aftershock interaction, *Science*, *259*(5092), 210–213.

Biegel, R. L., and C. G. Sammis (2004), Relating fault mechanics to fault zone structure, *Adv. Geophys*, *47*, 65–111.

Bizzarri, A. (2010), How to promote earthquake ruptures: Different nucleation strategies in a dynamic model with slip-weakening friction, *Bulletin of the Seismological Society of America*, *100*(3), 923–940.

Bizzarri, A. (2011), Dynamic seismic ruptures on melting fault zones, *Journal of Geophysical Research: Solid Earth*, *116*(B2).

Bizzarri, A., and M. Cocco (2005), 3D dynamic simulations of spontaneous rupture propagation governed by different constitutive laws with rake rotation allowed, *Annals of Geophysics*, *48*(2).

Bizzarri, A., and M. Cocco (2006a), A thermal pressurization model for the spontaneous dynamic rupture propagation on a three-dimensional fault: 1. methodological approach, *Journal of Geophysical Research: Solid Earth*, *111*(B5).

Bizzarri, A., and M. Cocco (2006b), A thermal pressurization model for the spontaneous dynamic rupture propagation on a three-dimensional fault: 2. traction evolution and dynamic parameters, *Journal of Geophysical Research: Solid Earth*, *111*(B5).

Brace, W., B. Paulding Jr, and C. Scholz (1966), Dilatancy in the fracture of crystalline rocks, *Journal of Geophysical Research*, *71*(16), 3939–3953.

Brodsky, E. E., J. J. Gilchrist, A. Sagy, and C. Collettini (2011), Faults smooth gradually as a function of slip, *Earth and Planetary Science Letters*, *302*(1), 185–193.

Brown, S. R., and C. H. Scholz (1985), Broad bandwidth study of the topography of natural rock surfaces, *J. Geophys. Res*, *90*(B14), 12,575–82.

Bruhat, L., Z. Fang, and E. M. Dunham (2016), Rupture complexity and the supershear transition on rough faults, *Journal of Geophysical Research: Solid Earth*, *121*(1), 210–224.

Bruhn, R. L. (1990), The mechanics of earthquakes and faulting, *Science*, *250*(4988), 1758–1760.

Caine, J. S., J. P. Evans, and C. B. Forster (1996), Fault zone architecture and permeability structure, *Geology*, *24*(11), 1025–1028.

Candela, T., F. Renard, M. Bouchon, A. Brouste, D. Marsan, J. Schmittbuhl, and C. Voisin (2009), Characterization of fault roughness at various scales: Implications of three-dimensional high resolution topography measurements, in *Mechanics, Structure and Evolution of Fault Zones*, pp. 1817–1851, Springer.

Candela, T., F. Renard, M. Bouchon, J. Schmittbuhl, and E. E. Brodsky (2011), Stress drop during earthquakes: effect of fault roughness scaling, *Bulletin of the Seismological Society of America*, *101*(5), 2369–2387.

Candela, T., F. Renard, Y. Klinger, K. Mair, J. Schmittbuhl, and E. E. Brodsky (2012), Roughness of fault surfaces over nine decades of length scales, *Journal of Geophysical Research: Solid Earth*, *117*(B8).

Chen, X., P. Shearer, and R. Abercrombie (2012), Spatial migration of earthquakes within seismic clusters in southern california: Evidence for fluid diffusion, *Journal of Geophysical Research: Solid Earth*, *117*(B4).

Chester, F., and J. M. Logan (1986), Implications for mechanical properties of brittle faults from observations of the punchbowl fault zone, california, *Pure and Applied Geophysics*, *124* (1-2), 79–106.

Chester, F., J. Chester, D. Kirschner, S. Schulz, and J. Evans (2004), Structure of large-displacement, strike-slip fault zones in the brittle continental crust, *Rheology and Deformation in the Lithosphere at Continental Margins*, *1*, 223–260.

Chester, F. M., and J. S. Chester (2000), Stress and deformation along wavy frictional faults, *Journal of Geophysical Research: Solid Earth*, *105* (B10), 23,421–23,430.

Chester, F. M., J. P. Evans, and R. L. Biegel (1993), Internal structure and weakening mechanisms of the san andreas fault, *Journal of Geophysical Research: Solid Earth*, *98* (B1), 771–786.

Cocco, M., and J. R. Rice (2002), Pore pressure and poroelasticity effects in coulomb stress analysis of earthquake interactions, *Journal of Geophysical Research: Solid Earth*, *107* (B2).

Cochran, E. S., Y.-G. Li, P. M. Shearer, S. Barbot, Y. Fialko, and J. E. Vidale (2009), Seismic and geodetic evidence for extensive, long-lived fault damage zones, *Geology*, *37* (4), 315–318.

Dalguer, L., K. Irikura, and J. Riera (2003), Simulation of tensile crack generation by three-dimensional dynamic shear rupture propagation during an earthquake, *Journal of Geophysical Research: Solid Earth*, *108* (B3).

Daub, E. G., and J. M. Carlson (2008), A constitutive model for fault gouge deformation in dynamic rupture simulations, *Journal of Geophysical Research: Solid Earth*, *113* (B12).

Daub, E. G., and J. M. Carlson (2010), Friction, fracture, and earthquakes, *Annu. Rev. Condens. Matter Phys.*, *1*(1), 397–418.

Day, S. M. (1982), Three-dimensional finite difference simulation of fault dynamics: rectangular faults with fixed rupture velocity, *Bulletin of the Seismological Society of America*, *72*(3), 705–727.

Di Toro, G., D. L. Goldsby, and T. E. Tullis (2004), Friction falls towards zero in quartz rock as slip velocity approaches seismic rates, *Nature*, *427*(6973), 436.

Di Toro, G., R. Han, T. Hirose, N. De Paola, S. Nielsen, K. Mizoguchi, F. Ferri, M. Cocco, and T. Shimamoto (2011), Fault lubrication during earthquakes, *Nature*, *471*(7339), 494–498.

Dieterich, J. H. (1979), Modeling of rock friction: 1. experimental results and constitutive equations, *Journal of Geophysical Research: Solid Earth*, *84*(B5), 2161–2168.

Dieterich, J. H., and D. E. Smith (2009), Nonplanar faults: Mechanics of slip and off-fault damage, *Pure and Applied Geophysics*, *166*(10-11), 1799–1815.

Duan, B. (2008), Effects of low-velocity fault zones on dynamic ruptures with nonelastic off-fault response, *Geophysical Research Letters*, *35*(4).

Duan, B., and D. D. Oglesby (2005), Multicycle dynamics of nonplanar strike-slip faults, *Journal of Geophysical Research: Solid Earth*, *110*(B3).

Dunham, E. M., and R. J. Archuleta (2005), Near-source ground motion from steady state dynamic rupture pulses, *Geophysical Research Letters*, *32*(3).

Dunham, E. M., D. Belanger, L. Cong, and J. E. Kozdon (2011a), Earthquake ruptures with strongly rate-weakening friction and off-fault plasticity, part 2: Nonplanar faults, *Bulletin of the Seismological Society of America*, *101*(5), 2308–2322.

Dunham, E. M., D. Belanger, L. Cong, and J. E. Kozdon (2011b), Earthquake ruptures with strongly rate-weakening friction and off-fault plasticity, part 1: Planar faults, *Bulletin of the Seismological Society of America*, *101*(5), 2296–2307.

El Hariri, M., R. E. Abercrombie, C. A. Rowe, and A. F. Do Nascimento (2010), The role of fluids in triggering earthquakes: observations from reservoir induced seismicity in Brazil, *Geophysical Journal International*, *181*(3), 1566–1574.

Erlingsson, S., and P. Einarsson (1989), Distance changes in the south Iceland seismic zone 1977-1984, *Jökull*, (39), 32–40.

Eshelby, J. D. (1957), The determination of the elastic field of an ellipsoidal inclusion, and related problems, *Proc. R. Soc. Lond. A*, *241*(1226), 376–396.

Fang, Z., and E. M. Dunham (2013), Additional shear resistance from fault roughness and stress levels on geometrically complex faults, *Journal of Geophysical Research: Solid Earth*, *118*(7), 3642–3654.

Faulkner, D., A. Lewis, and E. Rutter (2003), On the internal structure and mechanics of large strike-slip fault zones: field observations of the carboneras fault in southeastern Spain, *Tectonophysics*, *367*(3-4), 235–251.

Faulkner, D., C. Jackson, R. Lunn, R. Schlische, Z. Shipton, C. Wibberley, and M. Withjack (2010), A review of recent developments concerning the structure, mechanics and fluid flow properties of fault zones, *Journal of Structural Geology*, *32*(11), 1557–1575.

Faulkner, D., T. Mitchell, E. Jensen, and J. Cembrano (2011), Scaling of fault damage zones with displacement and the implications for fault growth processes, *Journal of Geophysical Research: Solid Earth*, *116*(B5).

Freed, A. M. (2005), Earthquake triggering by static, dynamic, and postseismic stress transfer, *Annu. Rev. Earth Planet. Sci.*, *33*, 335–367.

Gabriel, A.-A., J.-P. Ampuero, L. Dalguer, and P. M. Mai (2013), Source properties of dynamic rupture pulses with off-fault plasticity, *Journal of Geophysical Research: Solid Earth*, *118*(8), 4117–4126.

Gardner, J., and L. Knopoff (1974), Is the sequence of earthquakes in Southern California, with aftershocks removed, Poissonian?, *Bulletin of the Seismological Society of America*, *64*(5), 1363–1367.

Goldsby, D. L., and T. E. Tullis (2002), Low frictional strength of quartz rocks at sub-seismic slip rates, *Geophysical Research Letters*, *29*(17).

Goldsby, D. L., and T. E. Tullis (2011), Flash heating leads to low frictional strength of crustal rocks at earthquake slip rates, *Science*, *334*(6053), 216–218.

Gomberg, J., P. Bodin, and P. A. Reasenberg (2003), Observing earthquakes triggered in the near field by dynamic deformations, *Bulletin of the Seismological Society of America*, *93*(1), 118–138.

Gupta, H. K. (2002), A review of recent studies of triggered earthquakes by artificial water reservoirs with special emphasis on earthquakes in Koyna, India, *Earth-Science Reviews*, *58*(3-4), 279–310.

Gutenberg, B., and C. F. Richter (1944), Frequency of earthquakes in California, *Bulletin of the Seismological Society of America*, *34*(4), 185–188.

Hainzl, S. (2004), Seismicity patterns of earthquake swarms due to fluid intrusion and stress triggering, *Geophysical Journal International*, *159*(3), 1090–1096.

Hainzl, S., G. Zoeller, and R. Wang (2010), Impact of the receiver fault distribution on aftershock activity, *Journal of Geophysical Research: Solid Earth*, *115*(B5).

Han, R., T. Shimamoto, T. Hirose, J.-H. Ree, and J.-i. Ando (2007), Ultralow friction of carbonate faults caused by thermal decomposition, *Science*, *316*(5826), 878–881.

Hanks, T. C. (1977), Earthquake stress drops, ambient tectonic stresses and stresses that drive plate motions, in *Stress in the Earth*, pp. 441–458, Springer.

Hanks, T. C. (1992), Small earthquakes, tectonic forces, *Science*, *256*(5062), 1430–1432.

Hardebeck, J. (2010), Aftershocks are well aligned with the background stress field, contradicting the hypothesis of highly heterogeneous crustal stress, *Journal of Geophysical Research: Solid Earth*, *115*(B12).

Hardebeck, J. L. (2015), Comment on models of stochastic, spatially varying stress in the crust compatible with focal-mechanism data, and how stress inversions can be biased toward the stress rate by Deborah Elaine Smith and Thomas H. Heaton, *Bulletin of the Seismological Society of America*, *105*(1), 447–451.

Hardebeck, J. L., and P. M. Shearer (2002), A new method for determining first-motion focal mechanisms, *Bulletin of the Seismological Society of America*, *92*(6), 2264–2276.

Harris, R., et al. (2009), The SCEC/USGS dynamic earthquake rupture code verification exercise, *Seismological Research Letters*, *80*(1), 119–126.

Harris, R., et al. (2018), A suite of exercises for verifying dynamic earthquake rupture codes, *Seismological Research Letters*, *89*(3), 1146–1162.

Harris, R. A. (2004), Numerical simulations of large earthquakes: Dynamic rupture propagation on heterogeneous faults, in *Computational Earthquake Science Part II*, pp. 2171–2181, Springer.

Harris, R. A., and S. M. Day (1997), Effects of a low-velocity zone on a dynamic rupture, *Bulletin of the Seismological Society of America*, *87*(5), 1267–1280.

Harris, R. A., and R. W. Simpson (1992), Changes in static stress on southern california faults after the 1992 landers earthquake, *Nature*, *360*(6401), 251.

Hartzell, S., P. Liu, and C. Mendoza (1996), The 1994 northridge, california, earthquake: Investigation of rupture velocity, risetime, and high-frequency radiation, *Journal of Geophysical Research: Solid Earth*, *101*(B9), 20,091–20,108.

Hauksson, E. (2010), Spatial separation of large earthquakes, aftershocks, and background seismicity: Analysis of interseismic and coseismic seismicity patterns in southern California, in *Seismogenesis and Earthquake Forecasting: The Frank Evison Volume II*, pp. 125–143, Springer.

Hauksson, E. (2011), Crustal geophysics and seismicity in southern California, *Geophysical Journal International*, *186*(1), 82–98.

Helmstetter, A., Y. Y. Kagan, and D. D. Jackson (2005), Importance of small earthquakes for stress transfers and earthquake triggering, *Journal of Geophysical Research: Solid Earth*, *110*(B5).

Hill, D., et al. (1993), Seismicity remotely triggered by the magnitude 7.3 Landers, California, earthquake, *Science*, *260*(5114), 1617–1623.

Hill, D. P., F. Pollitz, and C. Newhall (2002), Earthquake-volcano interactions, *Physics Today*, *55*(11), 41–47.

Hirose, T., and M. Bystricky (2007), Extreme dynamic weakening of faults during dehydration by coseismic shear heating, *Geophysical Research Letters*, *34*(14).

Hirose, T., and T. Shimamoto (2005), Growth of molten zone as a mechanism of slip weakening of simulated faults in gabbro during frictional melting, *Journal of Geophysical Research: Solid Earth*, *110*(B5).

Hirth, G., and J. Tullis (1992), Dislocation creep regimes in quartz aggregates, *Journal of Structural Geology*, *14*(2), 145–159.

Ida, Y. (1972), Cohesive force across the tip of a longitudinal-shear crack and Griffith's specific surface energy, *Journal of Geophysical Research*, *77*(20), 3796–3805.

Ionescu, I. R., and M. Campillo (1999), Influence of the shape of the friction law and fault finiteness on the duration of initiation, *Journal of Geophysical Research: Solid Earth*, *104*(B2), 3013–3024.

Jaeger, J. C., N. G. Cook, and R. Zimmerman (2009), *Fundamentals of rock mechanics*, John Wiley & Sons.

Johri, M., E. M. Dunham, M. D. Zoback, and Z. Fang (2014), Predicting fault damage zones by modeling dynamic rupture propagation and comparison with field observations, *Journal of Geophysical Research: Solid Earth*, *119*(2), 1251–1272.

Kagan, Y. Y. (1994), Distribution of incremental static stress caused by earthquakes, *Nonlinear Processes in Geophysics*, *1*(2/3), 172–181.

Kilb, D., M. Ellis, J. Gomberg, and S. Davis (1997), On the origin of diverse aftershock mechanisms following the 1989 Loma Prieta earthquake, *Geophysical Journal International*, *128*(3), 557–570.

King, G. C., R. S. Stein, and J. Lin (1994), Static stress changes and the triggering of earthquakes, *Bulletin of the Seismological Society of America*, *84*(3), 935–953.

King, G. C., A. Hubert-Ferrari, S. S. Nalbant, B. Meyer, R. Armijo, and D. Bowman (2001), Coulomb interactions and the 17 August 1999 Izmit, Turkey earthquake, *Comptes Rendus de l'Académie des Sciences-Series IIA-Earth and Planetary Science*, *333*(9), 557–569.

Lapusta, N., J. R. Rice, Y. Ben-Zion, and G. Zheng (2000), Elastodynamic analysis for slow tectonic loading with spontaneous rupture episodes on faults with rate-and state-dependent friction, *Journal of Geophysical Research: Solid Earth*, *105*(B10), 23,765–23,789.

Lee, J.-J., and R. L. Bruhn (1996), Structural anisotropy of normal fault surfaces, *Journal of Structural Geology*, *18*(8), 1043–1059.

Lin, J., and R. S. Stein (2004), Stress triggering in thrust and subduction earthquakes and stress interaction between the southern san andreas and nearby thrust and strike-slip faults, *Journal of Geophysical Research: Solid Earth*, *109*(B2).

Lippiello, E., F. Giacco, W. Marzocchi, C. Godano, and L. De Arcangelis (2015), Mechanical origin of aftershocks, *Scientific reports*, *5*, 15,560.

Liu, J., K. Sieh, and E. Hauksson (2003), A structural interpretation of the aftershock cloud of the 1992 m w 7.3 landers earthquake, *Bulletin of the Seismological Society of America*, *93*(3), 1333–1344.

Lohman, R. B., and J. J. McGuire (2007), Earthquake swarms driven by aseismic creep in the Salton Trough, California, *Journal of Geophysical Research: Solid Earth*, *112*(B4).

Loret, B., and J. H. Prevost (1990), Dynamic strain localization in elasto-(visco-) plastic solids, part 1. general formulation and one-dimensional examples, *Computer Methods in Applied Mechanics and Engineering*, *83*(3), 247–273.

Ma, S., and G. C. Beroza (2008), Rupture dynamics on a bimaterial interface for dipping faults, *Bulletin of the Seismological Society of America*, *98*(4), 1642–1658.

Mai, P. M., and K. Thingbaijam (2014), Srcmod: An online database of finite-fault rupture models, *Seismological Research Letters*, *85*(6), 1348–1357.

Mai, P. M., P. Spudich, and J. Boatwright (2005), Hypocenter locations in finite-source rupture models, *Bulletin of the Seismological Society of America*, *95*(3), 965–980.

Mallman, E. P., and T. Parsons (2008), A global search for stress shadows, *Journal of Geophysical Research: Solid Earth*, *113*(B12).

Marsan, D. (2005), The role of small earthquakes in redistributing crustal elastic stress, *Geophysical Journal International*, *163*(1), 141–151.

Meier, M.-A., M. Werner, J. Woessner, and S. Wiemer (2014), A search for evidence of secondary static stress triggering during the 1992 Mw7. 3 Landers, California, earthquake sequence, *Journal of Geophysical Research: Solid Earth*, *119*(4), 3354–3370.

Michele, M., et al. (2016), The amatrice 2016 seismic sequence: a preliminary look at the mainshock and aftershocks distribution, *Annals of Geophysics*, *59*.

Mogi, K. (1971), Fracture and flow of rocks under high triaxial compression, *Journal of Geophysical Research*, *76*(5), 1255–1269.

Mogi, K. (1972), Fracture and flow of rocks, in *Developments in Geotectonics*, vol. 4, pp. 541–568, Elsevier.

Mogi, K. (1974), On the pressure dependence of strength of rocks and the coulomb fracture criterion, *Tectonophysics*, *21*(3), 273–285.

Myers, R., and A. Aydin (2004), The evolution of faults formed by shearing across joint zones in sandstone, *Journal of Structural Geology*, *26*(5), 947–966.

Nielsen, S. B., and L. Knopoff (1998), The equivalent strength of geometrical barriers to earthquakes, *Journal of Geophysical Research: Solid Earth*, *103*(B5), 9953–9965.

Noda, H., E. M. Dunham, and J. R. Rice (2009), Earthquake ruptures with thermal weakening and the operation of major faults at low overall stress levels, *Journal of Geophysical Research: Solid Earth*, *114*(B7).

Nur, A., and J. R. Booker (1972), Aftershocks caused by pore fluid flow?, *Science*, *175*(4024), 885–887.

Oglesby, D. D., and P. M. Mai (2012), Fault geometry, rupture dynamics and ground motion from potential earthquakes on the north anatolian fault under the sea of marmara, *Geophysical Journal International*, *188*(3), 1071–1087.

Okubo, P. G. (1989), Dynamic rupture modeling with laboratory-derived constitutive relations, *Journal of Geophysical Research: Solid Earth*, *94*(B9), 12,321–12,335.

Pankow, K. L., W. J. Arabasz, J. C. Pechmann, and S. J. Nava (2004), Triggered seismicity in utah from the 3 november 2002 denali fault earthquake, *Bulletin of the Seismological Society of America*, *94*(6B), S332–S347.

Parsons, T., R. S. Stein, R. W. Simpson, and P. A. Reasenberg (1999), Stress sensitivity of fault seismicity: A comparison between limited-offset oblique and major strike-slip faults, *Journal of Geophysical Research: Solid Earth*, *104*(B9), 20,183–20,202.

Pedersen, R., S. Jónsson, T. Árnadóttir, F. Sigmundsson, and K. L. Feigl (2003), Fault slip distribution of two June 2000 Mw 6. 5 earthquakes in South Iceland estimated from joint inversion of InSAR and GPS measurements, *Earth and Planetary Science Letters*, *213*(3-4), 487–502.

Perfettini, H., and J.-P. Avouac (2004), Postseismic relaxation driven by brittle creep: A possible mechanism to reconcile geodetic measurements and the decay rate of aftershocks, application to the Chi-Chi earthquake, Taiwan, *Journal of Geophysical Research: Solid Earth*, *109*(B2).

Perzyna, P. (1966), Fundamental problems in viscoplasticity, in *Advances in applied mechanics*, vol. 9, pp. 243–377, Elsevier.

Poliakov, A. N., R. Dmowska, and J. R. Rice (2002), Dynamic shear rupture interactions with fault bends and off-axis secondary faulting, *Journal of Geophysical Research: Solid Earth*, *107*(B11).

Power, W., and T. Tullis (1995), Review of the fractal character of natural fault surfaces with implications for friction and the evolution of fault zones, in *Fractals in the Earth Sciences*, pp. 89–105, Springer.

Power, W., T. Tullis, S. Brown, G. Boitnott, and C. Scholz (1987), Roughness of natural fault surfaces, *Geophysical Research Letters*, *14*(1), 29–32.

Powers, P. M., and T. H. Jordan (2010), Distribution of seismicity across strike-slip faults in California, *Journal of Geophysical Research: Solid Earth*, *115*(B5).

Renard, F., C. Voisin, D. Marsan, and J. Schmittbuhl (2006), High resolution three dimensional laser scanner measurements of a strike-slip fault quantify its morphological anisotropy at all scales, *Geophysical Research Letters*, *33*(4).

Rice, J. R. (1993), Spatio-temporal complexity of slip on a fault, *Journal of Geophysical Research: Solid Earth*, *98*(B6), 9885–9907.

Rice, J. R. (2006), Heating and weakening of faults during earthquake slip, *Journal of Geophysical Research: Solid Earth*, *111*(B5).

Rice, J. R., C. G. Sammis, and R. Parsons (2005), Off-fault secondary failure induced by a dynamic slip pulse, *Bulletin of the Seismological Society of America*, *95*(1), 109–134.

Rubin, A. M., and J.-P. Ampuero (2007), Aftershock asymmetry on a bimaterial interface, *Journal of Geophysical Research: Solid Earth*, *112*(B5).

Rubin, A. M., and D. Gillard (2000), Aftershock asymmetry/rupture directivity among central San Andreas fault microearthquakes, *Journal of Geophysical Research: Solid Earth*, *105*(B8), 19,095–19,109.

Rudnicki, J. W., and J. Rice (1975), Conditions for the localization of deformation in pressure-sensitive dilatant materials, *Journal of the Mechanics and Physics of Solids*, *23*(6), 371–394.

Ruina, A. (1983), Slip instability and state variable friction laws, *Journal of Geophysical Research: Solid Earth*, *88*(B12), 10,359–10,370.

Russ, J. C. (1994), *Fractal Surfaces.*, Plenum, New York.

Sagy, A., E. E. Brodsky, and G. J. Axen (2007), Evolution of fault-surface roughness with slip, *Geology*, *35*(3), 283–286.

Salichon, J., P. Lundgren, B. Delouis, and D. Giardini (2004), Slip history of the 16 October 1999 Mw 7.1 Hector Mine earthquake (California) from the inversion of InSAR, GPS, and teleseismic data, *Bulletin of the Seismological Society of America*, *94*(6), 2015–2027.

Schmedes, J., R. J. Archuleta, and D. Lavallée (2010), Correlation of earthquake source parameters inferred from dynamic rupture simulations, *Journal of Geophysical Research: Solid Earth*, *115*(B3).

Schmitt, S. V., P. Segall, and E. M. Dunham (2015), Nucleation and dynamic rupture on weakly stressed faults sustained by thermal pressurization, *Journal of Geophysical Research: Solid Earth*, *120*(11), 7606–7640.

Scholz, C. H. (1982), Scaling laws for large earthquakes: consequences for physical models, *Bulletin of the Seismological Society of America*, *72*(1), 1–14.

Scholz, C. H. (2002), *The mechanics of earthquakes and faulting*, Cambridge University Press.

Segou, M., and T. Parsons (2014), The stress shadow problem in physics-based aftershock forecasting: Does incorporation of secondary stress changes help?, *Geophysical Research Letters*, *41*(11), 3810–3817.

Shaw, B. E., K. Richards-Dinger, and J. H. Dieterich (2015), Deterministic model of earthquake clustering shows reduced stress drops for nearby aftershocks, *Geophysical Research Letters*, *42*(21), 9231–9238.

Shearer, P., E. Hauksson, and G. Lin (2005), Southern California hypocenter relocation with waveform cross-correlation, part 2: Results using source-specific station terms and cluster analysis, *Bulletin of the Seismological Society of America*, *95*(3), 904–915.

Shi, Z., and Y. Ben-Zion (2006), Dynamic rupture on a bimaterial interface governed by slip-weakening friction, *Geophysical Journal International*, *165*(2), 469–484.

Shi, Z., and S. M. Day (2013), Rupture dynamics and ground motion from three dimensional rough-fault simulations, *Journal of Geophysical Research: Solid Earth*, *118*(3), 1122–1141.

Sluys, L., and R. De Borst (1992), Wave propagation and localization in a rate-dependent cracked mediummodel formulation and one-dimensional examples, *International Jour-*

nal of Solids and Structures, *29*(23), 2945–2958.

Smith, D. E., and J. H. Dieterich (2010), Aftershock sequences modeled with 3-D stress heterogeneity and rate-state seismicity equations: Implications for crustal stress estimation, in *Seismogenesis and Earthquake Forecasting: The Frank Evison Volume II*, pp. 213–231, Springer.

Smith, D. E., and T. H. Heaton (2011), Models of stochastic, spatially varying stress in the crust compatible with focal-mechanism data, and how stress inversions can be biased toward the stress rate, *Bulletin of the Seismological Society of America*, *101*(3), 1396–1421.

Steacy, S., J. Gomberg, and M. Cocco (2005), Introduction to special section: Stress transfer, earthquake triggering, and time-dependent seismic hazard, *Journal of Geophysical Research: Solid Earth*, *110*(B5).

Stein, R. S. (1999), The role of stress transfer in earthquake occurrence, *Nature*, *402*(6762), 605.

Stein, R. S. (2003), Earthquake conversations, *Scientific American*, *288*(1), 72–79.

Stein, R. S., G. C. King, and J. Lin (1994), Stress triggering of the 1994 m= 6.7 northridge, california, earthquake by its predecessors, *Science*, *265*(5177), 1432–1435.

Suzuki, T., and T. Yamashita (2006), Nonlinear thermoporoelastic effects on dynamic earthquake rupture, *Journal of Geophysical Research: Solid Earth*, *111*(B3).

Templeton, E. L., and J. R. Rice (2008), Off-fault plasticity and earthquake rupture dynamics: 1. dry materials or neglect of fluid pressure changes, *Journal of Geophysical Research: Solid Earth*, *113*(B9).

Thatcher, W., and T. C. Hanks (1973), Source parameters of Southern California earthquakes, *Journal of Geophysical Research*, *78* (35), 8547–8576.

Tinti, E., A. Bizzarri, and M. Cocco (2005), Modeling the dynamic rupture propagation on heterogeneous faults with rate-and state-dependent friction, *Annals of Geophysics*, *48* (2).

Toda, S., R. S. Stein, P. A. Reasenberg, J. H. Dieterich, and A. Yoshida (1998), Stress transferred by the 1995 *Mw = 6.9* Kobe, Japan, shock: Effect on aftershocks and future earthquake probabilities, *Journal of Geophysical Research: Solid Earth*, *103* (B10), 24,543–24,565.

Toda, S., R. S. Stein, K. Richards-Dinger, and S. B. Bozkurt (2005), Forecasting the evolution of seismicity in southern california: Animations built on earthquake stress transfer, *Journal of Geophysical Research: Solid Earth*, *110* (B5).

Toda, S., J. Lin, M. Meghraoui, and R. S. Stein (2008), 12 May 2008 *M= 7.9* Wenchuan, China, earthquake calculated to increase failure stress and seismicity rate on three major fault systems, *Geophysical Research Letters*, *35* (17).

Tse, S. T., and J. R. Rice (1986), Crustal earthquake instability in relation to the depth variation of frictional slip properties, *Journal of Geophysical Research: Solid Earth*, *91* (B9), 9452–9472.

Tsutsumi, A., and T. Shimamoto (1997), High-velocity frictional properties of gabbro, *Geophysical Research Letters*, *24* (6), 699–702.

Vidale, J. E., and P. M. Shearer (2006), A survey of 71 earthquake bursts across Southern California: Exploring the role of pore fluid pressure fluctuations and aseismic slip as drivers, *Journal of Geophysical Research: Solid Earth*, *111* (B5).

Vidale, J. E., K. L. Boyle, and P. M. Shearer (2006), Crustal earthquake bursts in California and Japan: Their patterns and relation to volcanoes, *Geophysical research letters*, *33*(20).

Viesca, R. C., E. L. Templeton, and J. R. Rice (2008), Off-fault plasticity and earthquake rupture dynamics: 2. effects of fluid saturation, *Journal of Geophysical Research: Solid Earth*, *113*(B9).

Waite, G. P., and R. B. Smith (2002), Seismic evidence for fluid migration accompanying subsidence of the Yellowstone caldera, *Journal of Geophysical Research: Solid Earth*, *107*(B9).

Wald, D. J., and T. H. Heaton (1994), Spatial and temporal distribution of slip for the 1992 Landers, California, earthquake, *Bulletin of the Seismological Society of America*, *84*(3), 668–691.

Wald, D. J., D. V. Helmberger, and T. H. Heaton (1991), Rupture model of the 1989 loma prieta earthquake from the inversion of strong-motion and broadband teleseismic data, *Bulletin of the Seismological Society of America*, *81*(5), 1540–1572.

Waldhauser, F., and D. P. Schaff (2008), Large-scale relocation of two decades of Northern California seismicity using cross-correlation and double-difference methods, *Journal of Geophysical Research: Solid Earth*, *113*(B8).

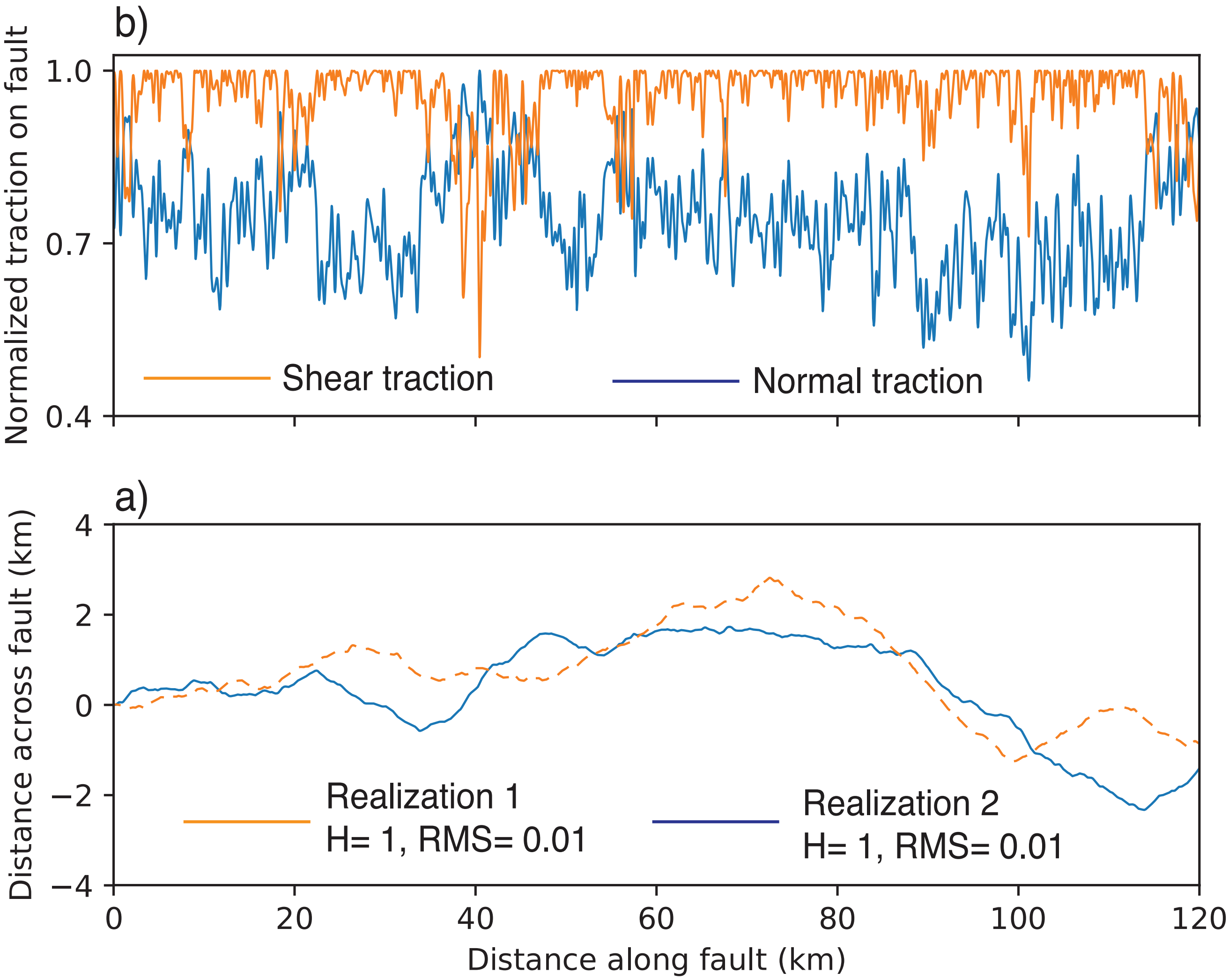

Figure 1. (a) Two different realizations of a self-similar rough fault with RMS height of 0.01. (b) The normal and shear traction values resolved on realization 2 of the rough fault profile shown in (a). The traction values along the the fault are heterogeneous even though the regional stresses are uniform. The heterogeneous tractions on the fault are solely due to the rough fault profile.

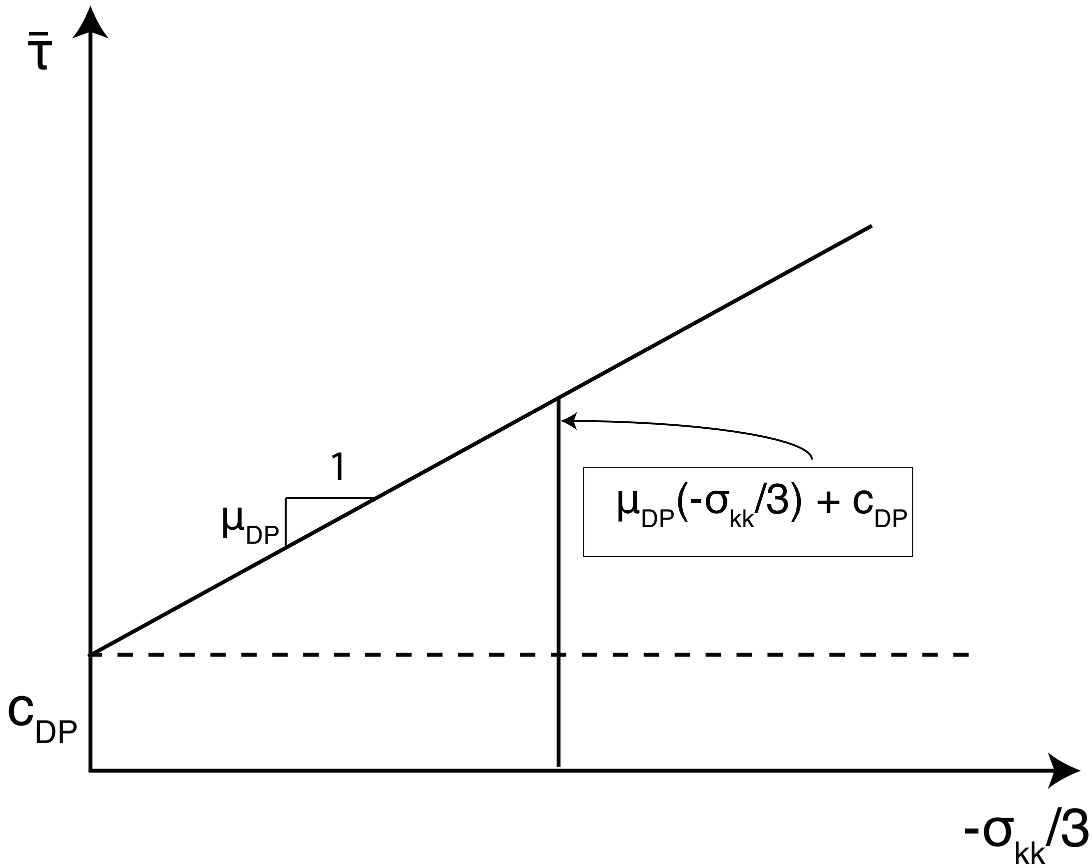

Figure 2. Yield criteria of Drucker-prager plasticity, which is used to model plastic deformation of rocks in numerical modeling of spontaneous earthquake rupture propagation. In our simulations, we assume a cohensionless off-fault material (i.e. $c_{DP} = 0$).

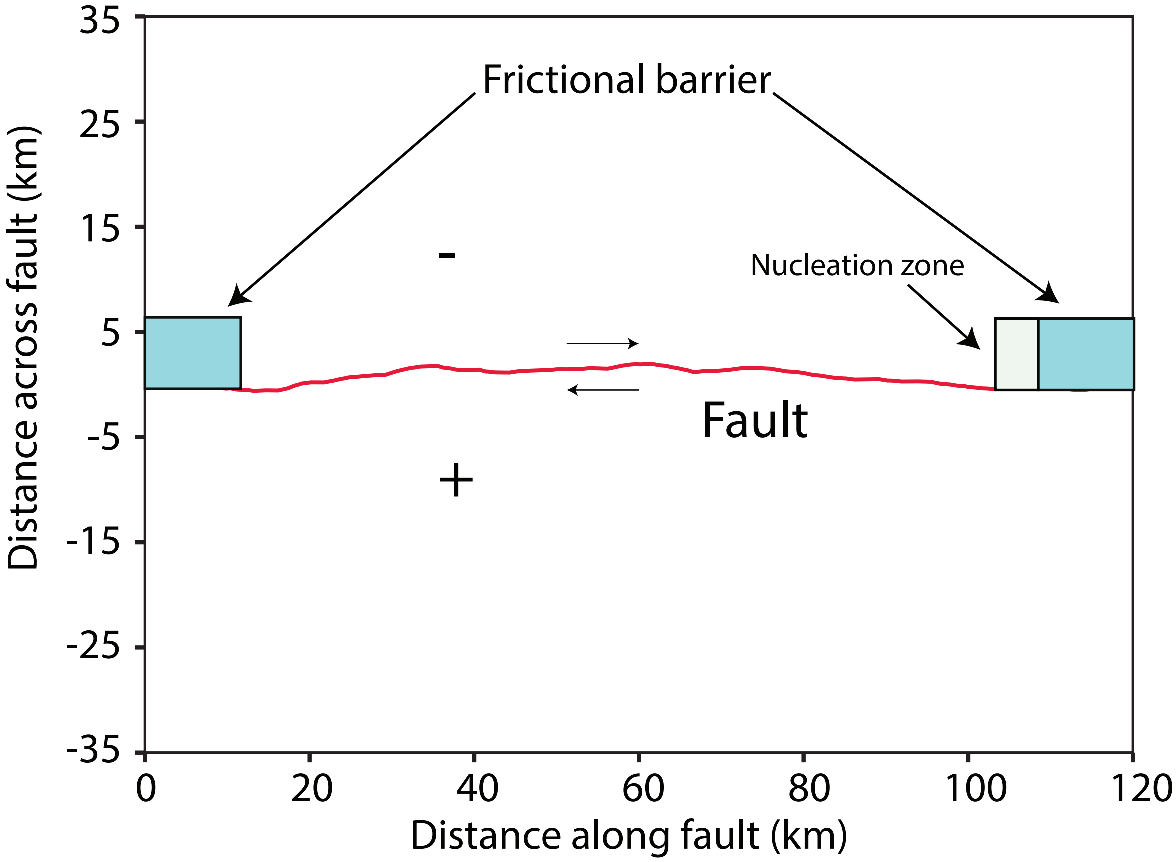

Figure 3. Modeling setup of our simulations. A self-similar rough fault profile is shown having a RMS height to wavelength ratio of 0.01. The minimum wavelength of the fault roughness is 500 m. The fault has a right lateral strike slip sense of slip, a length of 130 km, and a frictional barrier on either side. The barrier on the left is 15 km long, while the barrier on the right side starts at the edge of nucleation zone and extends to the edge of the simulation domain. The rupture always initiates on the right side of the fault. This results in accumulation of plastic deformation predominantly on one side of the fault. In our simulations, most of the plastic deformation occurs on the right side of the propagation of rupture direction. The extensional side is marked in the figure with '−' sign while the compressional side is marked with a '+' sign. In each rupture simulation, the domain setup remains the same while the profile of the rough fault changes.

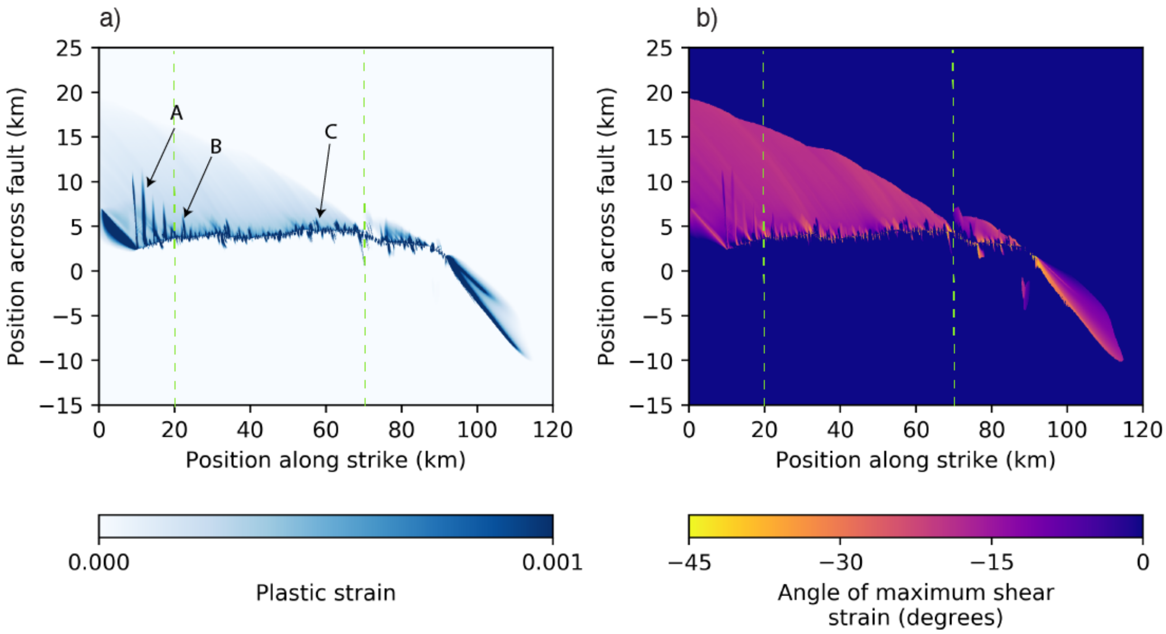

Figure 4. (a) Snapshot of the pattern of off-fault scalar plastic strain in the modeling sub-domain (20 to 70 km along fault and -15 to 25 km across fault distance) at time = 41.3 sec after the start of the rupture propagation. The geometric heterogeneity of the fault profile leads to a complex damage distribution across the main fault. (b) Estimated receiver fault orientations using the direction of maximum plastic shear strain. The orientations are heterogeneous in space, with orientations mostly within 25° of the main rupture trace. Note that the vertical scale in both (a) and (b) is exaggerated.

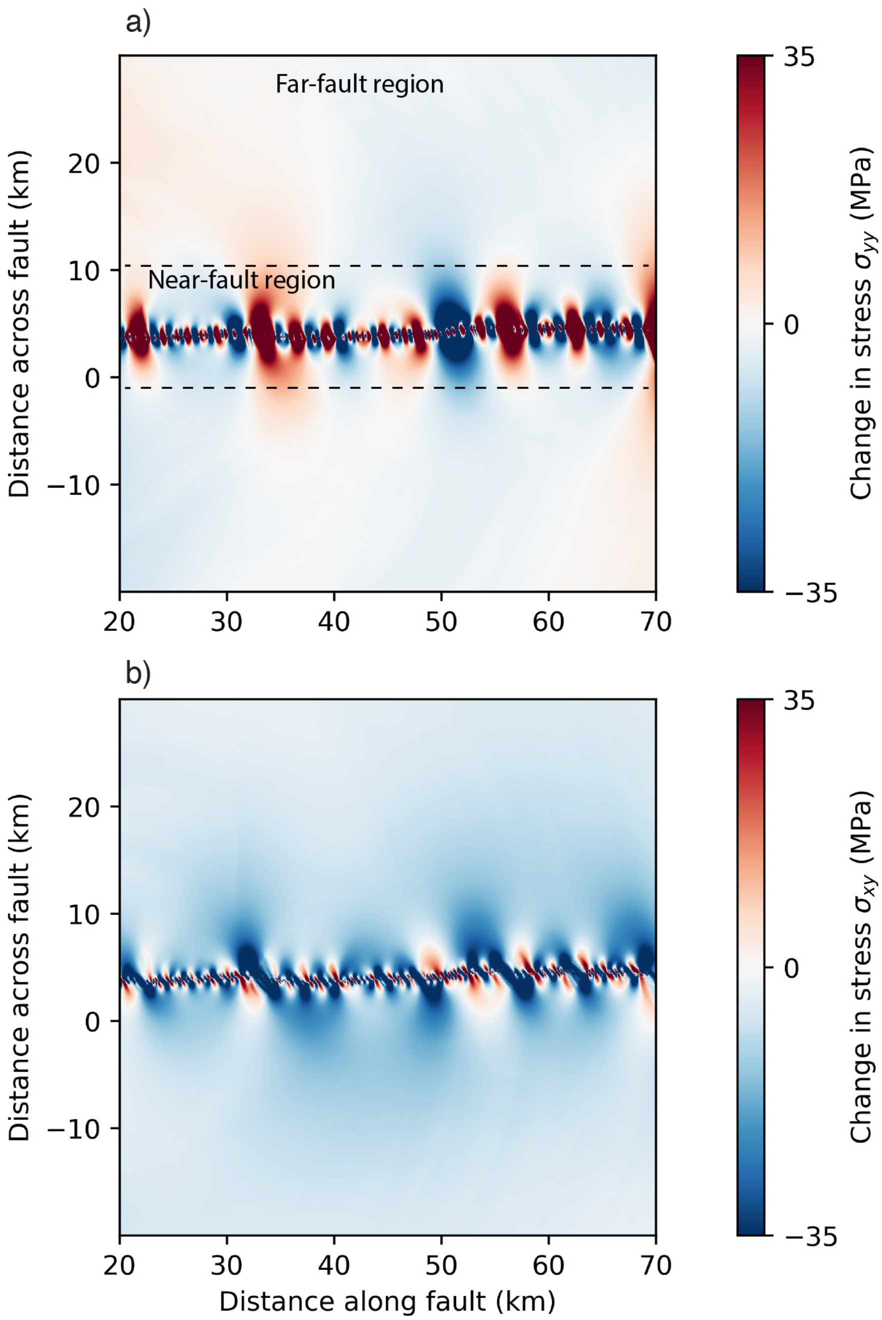

Figure 5. Change in stresses in the sub-domain region of the modeling domain for the fault profile shown in Fig 4. The simulation is run for a sufficient length of time (= 41.3 sec) such that there are no dynamic stresses related to the wave propagation and hence the stress change in the domain is present only due to static stress changes. a) Change in the normal stress in the modeling sub-domain. b) Change in the shear stress in the modeling sub-domain. The stress change in the near-fault region is highly complex, with most of the regions of the modeling sub-domain showing a decrease in the shear stress values.

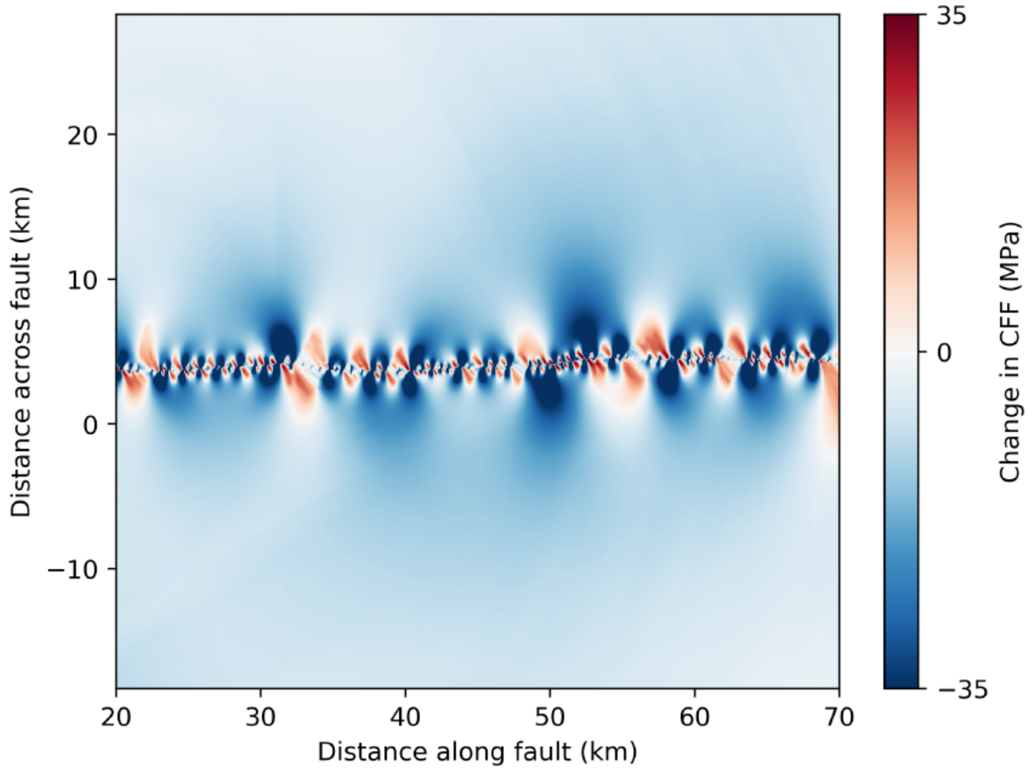

Figure 6. The CFF change calculated in the sub-domain region of the simulation for the fault profile shown in Fig 4. The CFF is calculated from the stress change values (both shear and normal stresses, shown in Fig. 4) as a result of dynamic earthquake slip on the rough fault. The calculations assume a frictional coefficient $\mu_\beta = 0.4$ and receiver fault orientations parallel to the mean host fault profile. The fault roughness of the fault profile results in a heterogeneous stress field within the rupture area of the main shock, resulting in an increased probability of occurrence of aftershocks within this area. Positive values of CFF change indicate that there is a higher probability of aftershock occurrence, while negative values of CFF change indicate regions of reduced probability of aftershocks. As can be seen, there is no obvious difference between the calculated CFF values in the extensional and compressional side of the fault. We also do an additional calculation of the CFF change on the extensional side of the fault with variable receiver fault orientations estimated using the direction of maximum plastic shear strain.

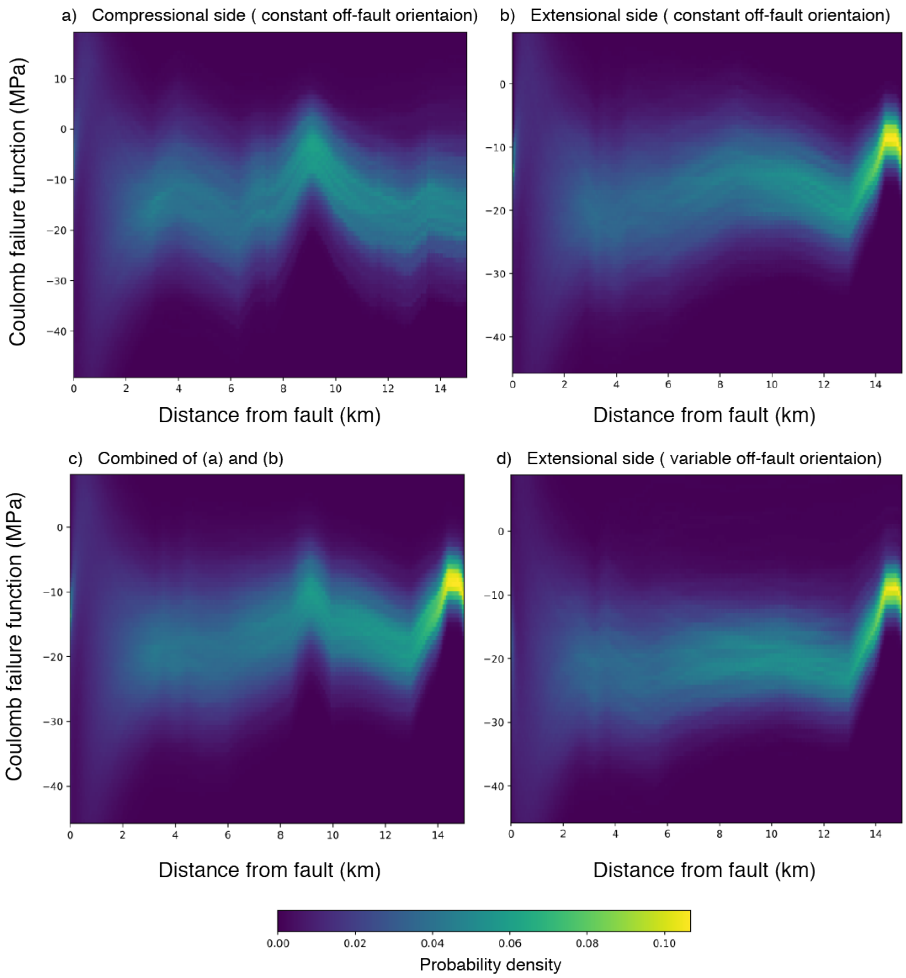

Figure 7. The probability density function (PDF) of the change in CFF values as a function of distance away from the fault. The CFF values are highly variable at distances very close to the fault, and collapse into a relatively very narrow range at greater distances from the fault. This behavior is due to the fact that in the near-fault region, fault roughness effects cause the stress to be heterogeneous. In the intermediate/far-field region, where the fault roughness effects are weaker, the CFF value spread is relatively narrow when compared to the near-fault region. (a) PDF of CFF change for the compressional side with parallel receiver fault orientations. (b) Same as (a) but for the extensional side. (c) Same as (a) but based on the combined values of (a) and (b). (d) Same as (b) but with variable receiver fault orientations. The optimum orientations of the receiver faults predominantly change the CFF values at the extreme of the distribution at a given distance. This is the reason that the difference between (b) and (d) is not obvious from point statistics but stands out when the spatial correlations (Fig. 8 and Fig. 9) are considered.

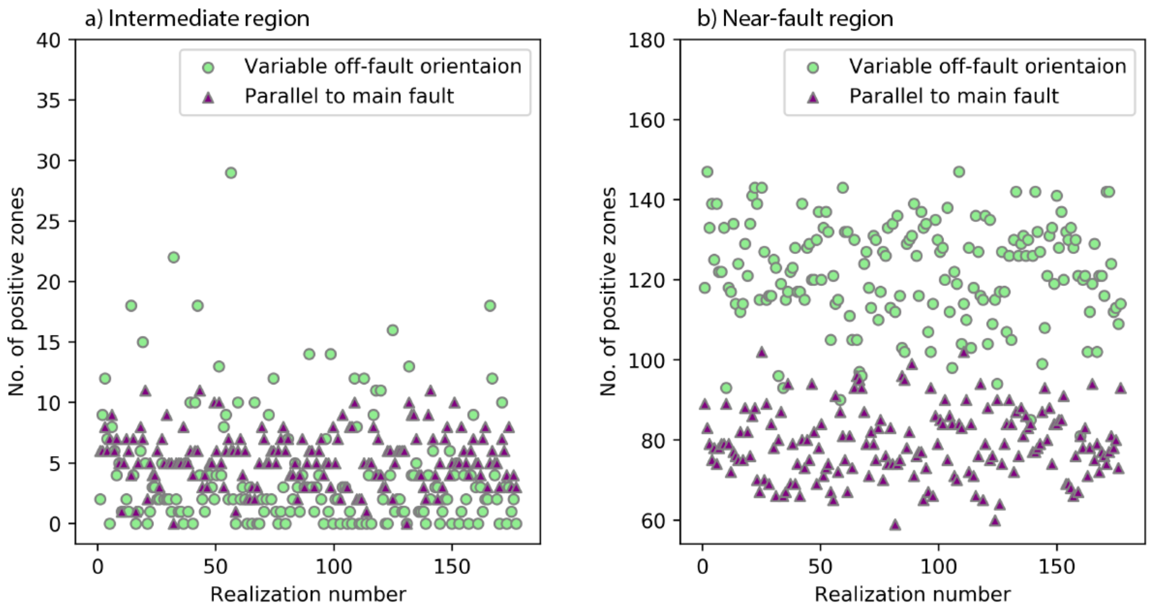

Figure 8. Figure shows total number of positive CFF zones calculated from all rupture simulations for the near-fault region and the intermediate region. (a) Number of positive zones calculated at 3.5 km away from the main fault using variable receiver fault orientations (circles) as well as parallel fault orientations (triangles). (b) Same as (a) but for positive zones 100 m away from fault. The orientations derived from the damage zone are clearly well aligned with the stress field in the near-fault region, while they lead to a greater variability in the number of zones in the intermediate region.

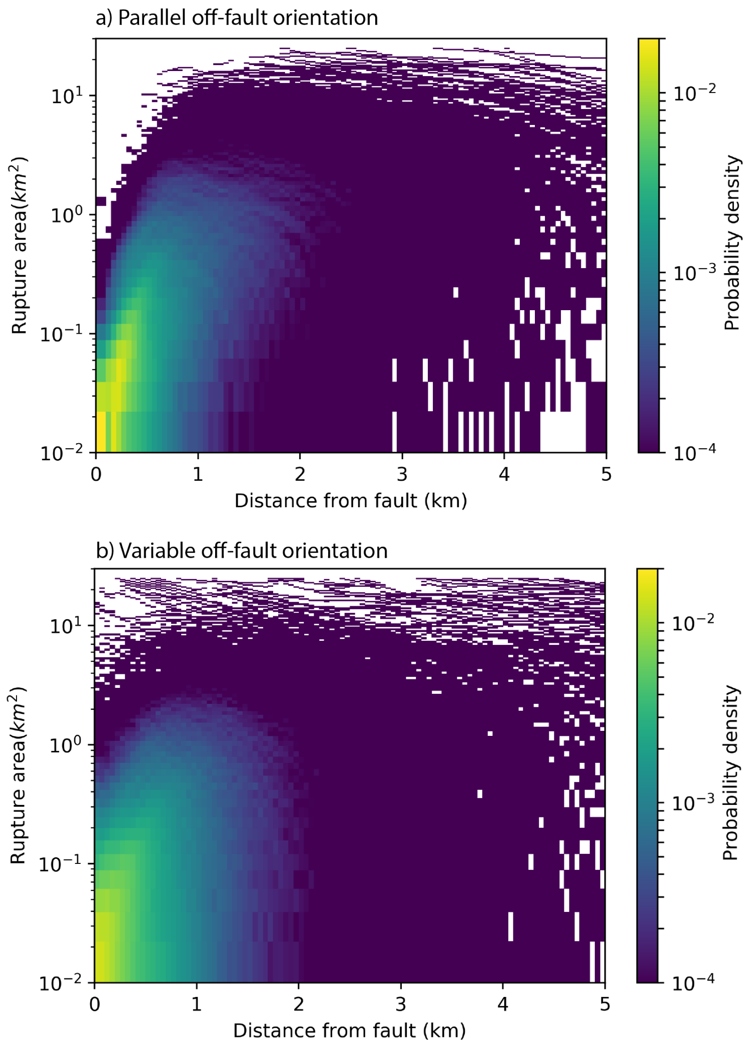

Figure 9. Areas of positive CFF zones versus distance from the fault. (a) Rupture areas calculated using parallel off-fault orientations. (b) Same as (a), but rupture areas are calculated using variable receiver fault orientations. The color scale in both (a) and (b) represents the joint PDF values of positive CFF area and distance. Our modeling results show that smaller zones are more probable close to the fault than large zones (both in (a) and (b)). This is because the stresses are more heterogeneous near the fault, leading to shorter correlation lengths and smaller zones. The larger rupture zones occur less frequently in the near-fault region as compared to the smaller zones. In the intermediate region, both smaller and larger rupture areas have equal probability of occurrence. Since a real aftershock does not always fill an entire positive CFF region, we expect many aftershocks with smaller rupture areas may present at intermediate distances. Furthermore, (b) is more complete in terms of probable rupture areas (fewer white spaces with PDF value = 0). This is because the optimal orientations of the receiver fault result

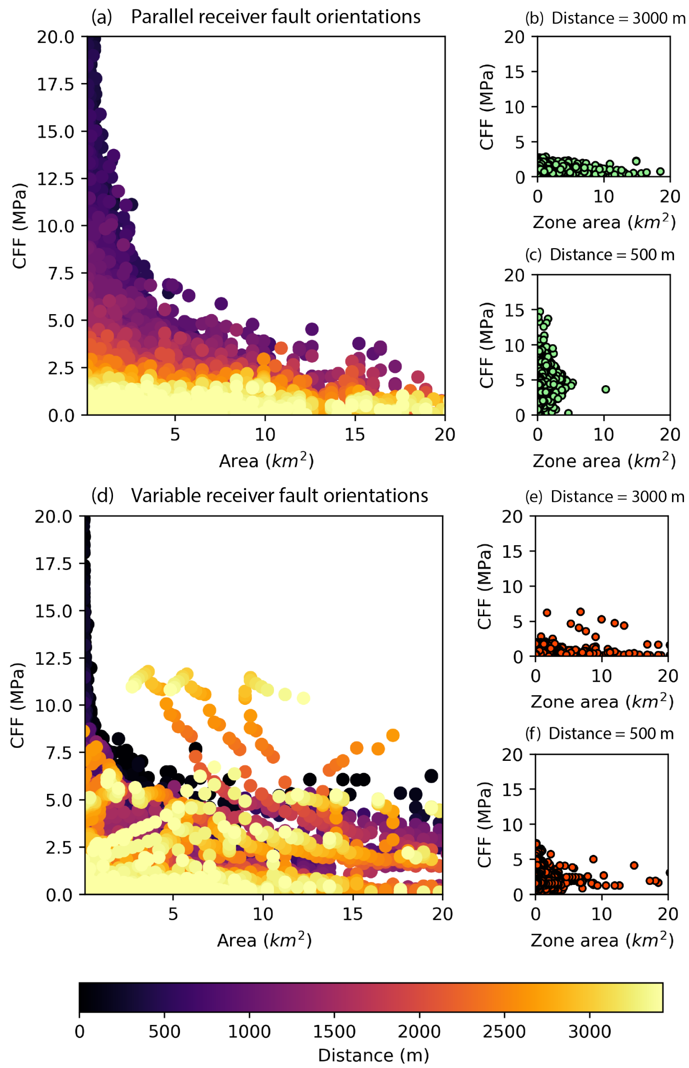

Figure 10. The plot shows the amplitude of CFF increase as a function of the zone area. (a) Rupture zone areas calculated using fault parallel receiver fault orientations, (d) Rupture zone areas calculated using variable receiver fault orientations. The color scale in both (a) and (d) represents the distance of each positive zone from the fault. (b) The amplitude of CFF increase as a function of the zone area calculated using similar receiver fault orientations for a distance of 3000 m away from fault. (c) The amplitude of CFF increase as a function of the zone area calculated using fault parallel receiver fault orientations for a distance of 500 m away from fault. (e) Same as (b), but the amplitude of CFF increase is calculated using variable receiver fault orientations. (f) Same as (c), but the amplitude of CFF increase as a function of the zone area is calculated using variable receiver fault orientations. As can be seen in (d), (e) and (f), the optimum orientations of the receiver fault tend to smooth the stress field, giving less extreme

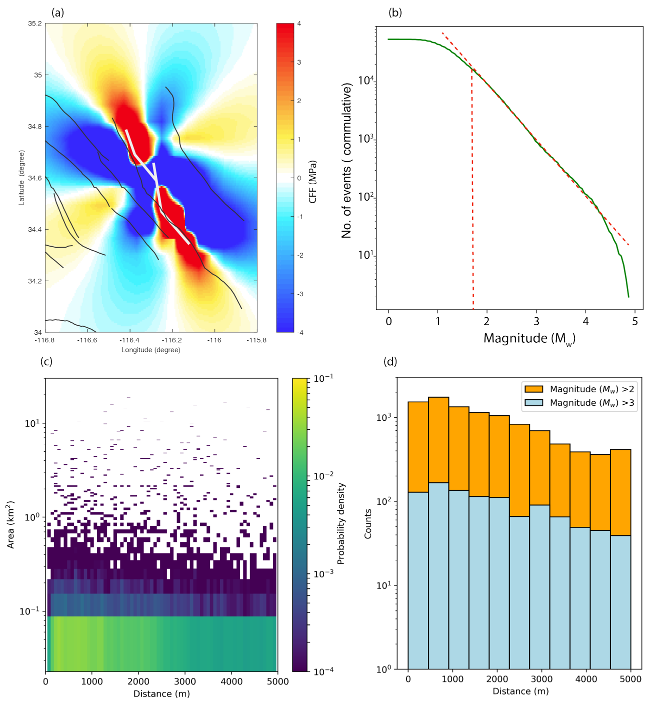

Figure 11. (a) The CFF calculated for the 1999 Hector Mine earthquake at 7.5 km focal depth, on the optimum orientations of strike slip receiver faults. We see two zones of positive CFF change while most of the near-fault region is dominated by a stress shadow. The white line shows the surface fault trace [*Salichon et al.*, 2004]. The black lines marks the trace of the known active faults present in the region. (b) The magnitude frequency distribution of the compiled dataset of aftershocks from five large earthquakes from the California region. These earthquakes include the 1984 Morgan Hill earthquake, the 1989 Loma Prieta earthquake, the 1992 Landers earthquake, the 1994 Northridge earthquake, and the 1999 Hector Mine earthquake. The magnitude frequency distribution follows the Gutenberg-Richter distribution. (c) Rupture areas and distance distribution for all the aftershocks occurring within 5 km from the main fault. The dataset is complied from 5 large earthquakes of California described in (b). (d) A comparison of histograms of aftershock distances from the fault plane for two different magnitude ranges for aftershock data shown in (b). The aftershocks follow the GR distribution at all distances from the fault with an order of magnitude more aftershocks with $M_w > 2$ than aftershocks with $M_w > 3$. Based on our model results, we suggest that this arises due to the roughness of the fault which produces positive CFF change zones of a variety of different lengths zones of positive stress change at all distances in the near-fault region.

Table 1. List of parameter values used in this study

	Parameter name	**Symbol used**	**Value**
Model Domain parameters			
	Domain length	X_{tot}	130 km
	Domain width	Y_{tot}	70 km
Material properties parameters			
	Compressional wave speed	V_p	6000 m/sec
	Shear wave speed	V_s	3464 m/sec
	DP internal friction parameter	μ_{DP}	0.5735
	DP plastic dilatancy parameter	β	0.2867
	DP viscosity parameter	η	0.2775 GPa.s
Friction law parameters			
	Static frictional coefficient	μ_s	0.7
	Dynamic frictional coefficient	μ_d	0.2
	Critical slip distance	D_c	0.4 m
Initial condition parameters			
	Stress	σ_{xx}	-100 MPa
	Stress	σ_{xy}	52.0 MPa
	Stress	σ_{yy}	-120 MPa
	Stress	σ_{zz}	-110 MPa
Fault Roughness parameters			
	Hurst exponent	H	1.0
	RMS height to wavelength ratio	γ	0.01